

High-frequency fluctuations of surface temperatures in an urban environment

Andreas Christen · Fred Meier · Dieter Scherer

Received: 28 May 2011 / Accepted: 1 September 2011 / Published online: 7 October 2011
© Springer-Verlag 2011

Abstract This study presents an attempt to resolve fluctuations in surface temperatures at scales of a few seconds to several minutes using time-sequential thermography (TST) from a ground-based platform. A scheme is presented to decompose a TST dataset into fluctuating, high-frequency, and long-term mean parts. To demonstrate the scheme's application, a set of four TST runs (day/night, leaves-on/leaves-off) recorded from a 125-m-high platform above a complex urban environment in Berlin, Germany is used. Fluctuations in surface temperatures of different urban facets are measured and related to surface properties (material and form) and possible error sources. A number of relationships were found: (1) Surfaces with surface temperatures that were significantly different from air temperature experienced the highest fluctuations. (2) With increasing surface temperature above (below) air temperature, surface temperature fluctuations experienced a stronger negative (positive) skewness. (3) Surface materials with lower thermal admittance

(lawns, leaves) showed higher fluctuations than surfaces with high thermal admittance (walls, roads). (4) Surface temperatures of emerged leaves fluctuate more compared to trees in a leaves-off situation. (5) In many cases, observed fluctuations were coherent across several neighboring pixels. The evidence from (1) to (5) suggests that atmospheric turbulence is a significant contributor to fluctuations. The study underlines the potential of using high-frequency thermal remote sensing in energy balance and turbulence studies at complex land–atmosphere interfaces.

1 Introduction

1.1 Fluctuations of surface temperatures at land–atmosphere interfaces

Surface temperatures of land surfaces are controlled by the surface energy balance (Monteith and Unsworth 2008). Surface temperatures vary as a consequence of radiative input and output (Q^*), changes in subsurface conduction of heat (Q_G) and changes in sensible (Q_H) and latent heat exchange (Q_E) with the atmosphere. Radiative input is relatively constant on short time periods (<1 h), the exceptions being sky conditions with broken clouds and situations underneath plant canopies where sun flecks cause rapid changes in short-wave irradiance (Chazdon 1988). However, at higher frequencies, in the order of seconds to minutes, surface temperatures are expected to respond to the turbulent sensible and latent heat flux densities in the atmosphere. The instantaneous wind field of atmospheric turbulence and the resulting changes of laminar

A. Christen (✉)
Department of Geography, University of British Columbia,
1984 West Mall, Vancouver, BC, V6T 1Z2, Canada
e-mail: andreas.christen@ubc.ca

F. Meier · D. Scherer
Department of Ecology, Technische Universität Berlin,
Rothenburgstraße 12, 12165 Berlin, Germany

F. Meier
e-mail: fred.meier@tu-berlin.de

D. Scherer
e-mail: dieter.scherer@tu-berlin.de

boundary layer thickness are expected to control temperature fluctuations and cause them to respond to atmospheric heat surplus or deficits (carried by turbulent eddies) on the same length and time scales as the atmospheric motions themselves.

Paw-U et al. (1992) operated a directional infrared thermometer at a nominal frequency of 10 Hz over a maize canopy and identified ramp structures in the surface temperature signal of the crop that were significantly correlated with simultaneously measured fluctuations in air temperature above the canopy. The magnitude of surface temperature ramps was, however, significantly smaller than the air temperature ramps. The ramps in the surface temperature signal reflect the abrupt replacement of progressively warmed (or cooled) near-surface air with well-mixed cool (warm) air from aloft driven by coherent eddies in the turbulent flow. Katul et al. (1998) investigated the temporal variability in surface temperature fluctuations of a forest clearing. They linked fluctuations in surface temperature to turbulent velocities in the overlaying atmosphere. They measured large fluctuations in surface temperatures in the order of 2 K which scaled with inactive eddy motion in the atmospheric boundary layer. Ballard et al. (2004) measured high-frequency fluctuations of directional thermal radiance in a grass canopy at 1-s to 5-min intervals and hypothesized that turbulent mixing plays a dominant role in explaining high-frequency traces.

Surface temperature fluctuations due to turbulent exchange are expected to depend on the surface material's thermal properties and the efficiency of the atmosphere to exchange heat through the laminar and turbulent boundary layers. The latter process is driven by atmospheric dynamics, which are in turn controlled in part by the surface's form (roughness).

Our hypothesis is that surface temperature fluctuations on various facets of a complex land–atmosphere interface are driven by the high-frequency dynamics of the instantaneous surface–atmosphere exchange. For longer integration periods (>20 min to 2 h), we suggest that spatial differences in mean surface temperature between facets and trends in mean surface temperature are controlled by different radiative input and conductive storage fluxes which, in turn, are controlled by surface material (albedo, thermal properties) and form (orientation, sky view factor, solar geometry, porosity). At higher frequencies (<20 min), however, surface temperature fluctuations can be expected to follow the discussed dynamic effects of wind (i.e., turbulent exchange). As a practical approach, we hence suggest to separating the spatial field of measured surface

temperatures conceptually into a mean (trend) and a fluctuating (high-frequency) part to assist us in quantifying the forcing processes acting on different time scales.

1.2 The use of time-sequential thermography

State-of-the-art thermal infrared (TIR) cameras allow a simultaneous sampling of spatial and temporal changes of surface temperatures by recording a time series (t) of thermal images ($\mathbf{x} = x, y$). We will refer to this as time-sequential thermography (TST; Hoyano et al. 1999). TST is typically restricted to fixed ground-based platforms with a directional field of view (FOV), as sensors on airborne or satellite platforms do not provide enough temporal repetition and/or geometric resolution to resolve small-scale and short-term changes that are potentially caused by a turbulent atmosphere.

1.2.1 TST in urban environments

TST in previous research on urban surfaces was mostly motivated by either (a) the potential to infer thermal properties of the urban surface, (b) to determine terms of the surface energy balance, or (c) to analyze building environment heat transfer. Most studies reported in the peer-reviewed literature use TST to resolve spatial differences in mean temperature and warming and cooling rates from hourly to diurnal time steps. Hoyano et al. (1999) used TST runs of buildings over 24 h recorded at 1-min intervals to infer sensible heat flux density of individual building facets. Sugawara et al. (2001) and Chudnovsky et al. (2004) used fixed TIR cameras on top of high-rise buildings (>100 m) that were operated at intervals of 5 and 60 min to estimate thermal properties of urban surface facets at the neighborhood scale. Meier et al. (2010) used TST recorded at 1-min intervals to investigate thermal dynamics in an urban courtyard over 2 days and used the attenuation of thermal persistence effects (e.g., shadow) in order to derive surface thermal admittance. All studies cited above analyzed and discussed temporal variation on time scales typically larger than those of turbulent length scales.

1.2.2 TST in vegetation studies

In non-urban ecosystems, TST has been applied to study temporal and spatial variations in surface temperatures of grassland (e.g., Shimoda and Oikawa 2008, TST at 5-min intervals) or the estimation of biomass

heat storage (e.g., Garai et al. 2010, TST at 2-min intervals). Higher-frequency analysis has been used in the laboratory to study stomatal regulation and transpiration of individual leaves (e.g., Jones 1999, TST at 1-min intervals). Leuzinger and Körner (2007) investigated thermal regulation of leaf temperatures in a forest canopy using TST at 5-s intervals. They observed fluctuations in leaf temperatures up to 2 K that remained entirely unexplained, but also concluded that the unexplained fluctuations correlated poorly against measured wind speed. They do not rule out that wind causes the observed fluctuations but argue that the actual turbulent patterns experienced by the sampled trees may have deviated substantially from their single-point anemometer. Ballard et al. (2004) used TST to study grass surface temperatures at 1.3 m above the canopy at a 20-s interval and report qualitatively a “rapid effect of cooling from the wind is easily noticeable” in their TST runs.

The specific objectives of the current contribution are to (a) present a scheme to decompose a signal of measured apparent surface temperatures by time-sequential thermography into a high-frequency fluctuating and a long-term mean part, (b) apply the decomposition scheme to a set of time-sequential thermography runs from a complex urban environment that is composed of many different facets and surface materials, and (3) quantify surface temperature fluctuations of the different urban facets and relate them to surface properties, quantify possible instrumental error sources and effects along the line of sight (LOS). To simplify the discussion, in this contribution we will use the term “temperature” and the symbol T for “apparent surface temperatures” with a surface emissivity of $\varepsilon = 1.0$. If we refer to air temperature, or corrected surface temperatures, this will be explicitly noted.

2 Methods

2.1 Experimental setup

To address objectives (b) and (c), this contribution builds upon data sampled by a TIR camera that recorded temperature fluctuations in a complex urban setting. We use data from an urban environment because this provides the opportunity to simultaneously sample a large spectrum of various land-surface materials and 3-D form (height above ground, slope, azimuth, vegetation, and artificial materials) under the same meteorological forcing.

2.1.1 Thermal camera

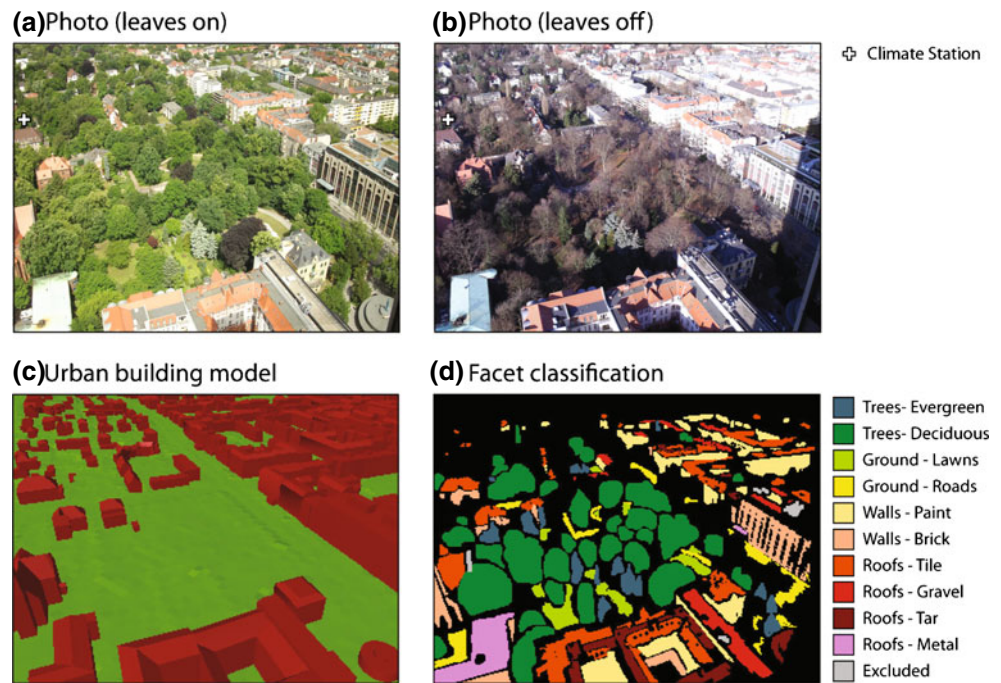
The TIR camera used in this study is a VarioCAM[®] head (InfraTec GmbH, Dresden, Germany) that was operated at 1 Hz. The camera uses an uncooled microbolometer focal plane array (320 × 240 pixels) that is thermally stabilized with a Peltier element. It is recording the signal at a resolution of 16 bit (thermal resolution 0.08 K at 30°C) with an accuracy of 2% (InfraTec 2005). The spectral range of the camera’s sensitivity is between 7.5 and 14.0 μm. The camera’s aperture is protected by a polyethylene foil with an estimated transmissivity of $\tau_{\text{foil}} = 0.75$ in the sensitive range, which is considered in the radiance-to-temperature conversion. The array is protected by an encapsulation (IP 65), and the camera is enclosed in an environmental enclosure that hosts a ventilation and heating system to avoid strong temperature fluctuations. During operation, case temperature was continuously monitored. Every 6 s, all microbolometer elements were homogenized (shutter), and the camera case temperature was stored in order to use the optimized radiance-to-temperature calibration parameters and to avoid drift effects. The calibration parameters for the camera system were determined by the manufacturer using blackbody temperatures. The resulting time-series were corrected in post-processing for geometry (lens distortion) and for lens vignetting/narcissus effects before any further post-processing steps. All corrections are described in detail in Meier et al. (2011).

2.1.2 Field of view

The TIR camera was installed on top of an isolated high-rise building overseeing part of the city of Berlin, Germany (52.4556° N, 13.3200° E, WGS-84). The camera was mounted on a boom at a height of 125 m above ground level 3 m off the roof’s edge. The original FOV of the camera is 64 × 50° and covers an area of approximately 0.3 km². As a result of the geometric correction, the FOV in the analysis was cropped to 57 × 44°. TST runs were recorded with a fixed FOV oriented toward northwest (325°) and inclined by 59° from the nadir (FOV ranges between 36.3° and 81.8° from the nadir). Due to the oblique view, the sensor-target distance varies between 125 and 700 m (median 234 m), which corresponds to a geometric resolution between 0.5 and 2.5 m for the instantaneous field of view (IFOV) of 3.6 mrad.

Urban cover and form in the FOV is documented in Fig. 1. The underlying terrain has a gentle slope of about 1° from the foreground (SE, 42 m a.s.l.) to the image background (NW, 65 m a.s.l.). The FOV is

Fig. 1 Field of view of thermal camera for **a** leaves on, **b** leaves off, **c** digital building model, and **d** surface classification



characterized by a high fraction of urban vegetation and contrasting building densities. The upper right (northern part) is dominated by five- to six-story buildings enclosing courtyards. The center and the left side (south) include a park with mature trees and detached low and mid-rise residential houses. Figure 1c shows modeled buildings and ground elevation in the camera's field of view (in absence of vegetation). The dataset was calculated from a 3-D building vector model format (Kolbe 2009) in combination with a digital ground model (DGM). The building model and the DGM combined results into a digital surface model (DSM), which will be further used in the analysis.

Trees found in the FOV are dominantly deciduous that include *Acer platanoides*, *Acer pseudoplatanus*, *Fagus sylvatica*, *Populus nigra*, *Quercus robur*, *Tilia* sp. The FOV also shows a few evergreen trees (approximately 10% of all trees, *Taxus baccata*, *Pinus sylvestris*, *Abies procera*). Tree height varies between 10 and 30 m. Figure 1a and b shows the contrasting surface of the leaves-on and leaves-off situation.

2.1.3 Climate measurements

Downward short-wave $\downarrow E_{SW}$ and long-wave radiation $\downarrow E_{LW}$ (CM3 and CG 3, Kipp & Zonen, Delft, the Netherlands), air temperature T_{air} , and relative humidity (RH; HMP45A, Vaisala, Vantaa, Finland) are measured on top of the isolated high-rise building. Additionally, a fast anemometer/thermometer

(USA-1, Metek GmbH, Elmshorn, Germany) and hygrometer (Li-7500, Licor Inc., Lincoln, NK, USA) were operated at the same location. Within the FOV, at a horizontal distance of 300 m from the high-rise building (52.4568° N, 13.3161° E, WGS-84, "Climate Station" in Fig. 1), T_{air} and RH were measured at ground level (2 m) underneath a relatively open tree canopy and again 3.5 m above an exposed 19 m pitched roof (both HMP45A, Vaisala, Vantaa, Finland). Wind velocity/direction (Lambrecht GmbH, Göttingen, Germany) was measured 4 m above the same roof.

2.1.4 TST runs

In April 2009, four 80-min runs were recorded at 1 Hz. The weather conditions during the four runs and for the preceding 24 h are summarized in Table 1. Two of the runs, D1 and N1, are from early April when leaves of the deciduous trees have not yet emerged ("leaves-off"), and hence, more ground and building walls are visible. The second set, runs D2 and N2 ("leaves-on"), is from late April 2009 when leaves emerged and a closed canopy formed over the park. All runs were recorded under cloudless skies. Daytime runs are characterized by high downward short-wave radiation with averages of 634 (D1) and 780 (D2) $W m^{-2}$. The wind velocity was relatively low and ranged between 2.3 and 2.6 $m s^{-1}$ at 23 m a.g.l. and between 1.6 and 2.9 $m s^{-1}$ at 125 m a.g.l.

Table 1 Weather conditions during the four runs

Run			Day		Night	
			D1	D2	N1	N2
Date			Leaves-off April 7, 2009	Leaves-on April 20, 2009	Leaves-off April 6, 2009	Leaves-on April 20, 2009
Time		CET	11:00–12:20	11:48–13:08	20:37–21:57	21:00–22:20
Short-wave incoming	80 min average	W m ⁻²	634	780	0	0
	Preceding 24 h total	MJ m ⁻² day ⁻¹	19.5	25.8	22.2	25.8
Long-wave incoming	80 min average	W m ⁻²	317	286	292	269
	Preceding 24 h total	MJ m ⁻² day ⁻¹	25.6	23.2	24.4	23.4
Wind	23 m	m s ⁻¹	2.6	2.3	2.3	2.4
	125 m	m s ⁻¹	1.6	1.8	2.9	2.9
Wind direction	23 m	° from N	125	66	96	39
Air temperature	2 m	°C	20.4	16.7	12.5	11.8
	125 m	°C	18.8	16.3	13.1	12.4
Standard deviation	125 m	K	0.63	1.12	0.19	0.15
Relative humidity	2 m	%	49.8	36.7	60.1	52.6
	125 m	%	47.5	24.5	57.2	41.8
Standard deviation	125 m	g m ⁻³	0.0063	0.0061	0.0047	0.0043

Standard deviations of air temperature and humidity are based on 10 Hz measurements averaged over 10 min

2.2 Analysis of TST data

2.2.1 Decomposition schemes

The TST runs of $T(\mathbf{x}, t)$ were decomposed in post-processing using spatial and temporal averaging operators with the goal to separate high-frequency fluctuations in temperatures from the mean patterns and trends. A temporal averaging operator is written using an overbar. For example, the temporal average of the temperature $T(\mathbf{x}, t)$ of a single pixel in the image is $\overline{T}(\mathbf{x})$:

$$\overline{T}(\mathbf{x}) = \frac{1}{N} \sum_{t=0}^N T(\mathbf{x}, t) \tag{1}$$

A spatial average is written using angle brackets, so the average temperature of a spatial subset or the entire image is $\langle T \rangle(t)$:

$$\langle T \rangle(t) = \frac{1}{M} \sum_{\mathbf{x}=0}^M T(\mathbf{x}, t) \tag{2}$$

This short-hand notation is in accordance with the common notation in atmospheric turbulence theory (Raupach and Shaw 1982), although it should be noted that the spatial averaging operator in this application does not equally weight surface areas due to the distorted image geometry (IFOV vs. distance) and so this term is not equal to the spatially averaged complete surface temperature as defined by Voogt and Oke (1997).

We define departures at a time step t from the temporal average using the prime symbol

$$T'(t) = T(t) - \overline{T} \tag{3}$$

In analogy, we suggest a dot-in-a-box symbol (\square) to denote the deviation of a pixel at location \mathbf{x} from the spatial average of a region or an entire image:

$$T^{\square}(\mathbf{x}) = T(\mathbf{x}) - \langle T \rangle \tag{4}$$

The time-sequential thermography images were decomposed following two schemes: firstly according to the inner-temporal outer-spatial scheme:

$$T(\mathbf{x}, t) = T'(\mathbf{x}, t) + \overline{T^{\square}}(\mathbf{x}) + \langle \overline{T} \rangle \tag{5}$$

The left-hand side is the instantaneous temperature as measured by the thermal camera. $T'(\mathbf{x}, t)$ is the temporal departure of the instantaneous temperature of a pixel from its (temporal) average temperature. We call this term *ftrend*. *ftrend* quantifies how the temperature of a pixel compares to its own long-term average temperature and is a function of both time and space. The second term, $\overline{T^{\square}}(\mathbf{x})$, is the spatial departure of the temporally averaged temperature of a pixel from the entire spatiotemporal average of the time sequence. We call this term *mpattern*. *mpattern* is a 2-D image (describing the entire run) that shows the pixel's temperature departure from the image mean, i.e., if a pixel is on average warmer or cooler than the entire image. The last term in Eq. 5, $\langle \overline{T} \rangle$, is the spatiotemporal average of the time-sequential images, which is a single scalar that

denotes the average temperature of the entire run of all pixels. We name the last term *mtotal*. All terms and their respective names are summarized in Table 2.

In analogy, we can also form an inner-spatial outer-temporal decomposition:

$$T(\mathbf{x}, t) = T^{\square}(\mathbf{x}, t) + \langle T \rangle'(t) + \overline{\langle T \rangle} \tag{6}$$

The left-hand side is again the instantaneous temperature image, similar to Eq. 5. $T^{\square}(\mathbf{x}, t)$ is the spatial departure of the instantaneous temperature of a pixel from the spatial average of the instantaneous image. We name this term *fpattern*. *fpattern* tells us how the temperature of a pixel compares to the temperature of spatially separated pixels at the same time. *fpattern* is also a function of time and space. The second term in Eq. 6, $\langle T \rangle'(t)$, is the temporal departure of the spatial average temperature of an instantaneous image from the spatiotemporal average of the time sequence. We call this term *mtrend*. This is a time series with a single value per time step. It tells us if an image is generally warmer or cooler than the entire time sequence and hence will typically show the warming/cooling trend of the entire time sequence. As calibration is applied every 6 s, part of the signal in *mtrend* is expected to come from the drift of the entire microbolometer focal plane array. By subtracting *mtrend*, errors from sensor drift can be reduced. The last term in Eq. 6 again is the spatiotemporal average of the time-sequential images, i.e., *mtotal*. Note that by definition of an average, it follows: $\overline{\langle T \rangle} = \langle \overline{T} \rangle$.

Combining Eqs. 5 and 6 gives:

$$T'(\mathbf{x}, t) + \overline{T^{\square}}(\mathbf{x}) + \langle \overline{T} \rangle = T^{\square}(\mathbf{x}, t) + \langle T \rangle'(t) + \overline{\langle T \rangle} \tag{7}$$

As the spatiotemporal average is the same in both cases, Eq. 7 simplifies to:

$$T'(\mathbf{x}, t) + \overline{T^{\square}}(\mathbf{x}) = T^{\square}(\mathbf{x}, t) + \langle T \rangle'(t) \tag{8}$$

By combining the two averaging schemes, we can form a total fluctuating component, which is the deviation from both the spatial and temporal average. This term will be called *ftotal*.

$$ftotal = T(\mathbf{x}, t) - \overline{T^{\square}}(\mathbf{x}) - \langle T \rangle'(t) - \overline{\langle T \rangle} \tag{9}$$

Based on Eqs. 5 and 6, *ftotal* can be rewritten as

$$ftotal = T^{\square}(\mathbf{x}, t) - \overline{T^{\square}}(\mathbf{x}) = T'(\mathbf{x}, t) - \langle T \rangle'(t) \tag{10}$$

ftotal can be considered as the high-frequency fluctuation of a pixel from the spatiotemporal mean. It has long-term warming (or cooling) removed as it shows only the deviation from its own average temperature. Further, *ftotal* eliminates changes in temperature that affect the entire image. Hence, this term is very useful as it eliminates instrumental effects (shutter) that can affect the entire microbolometer focal plane array.

It is important to note that the scheme introduced here, and the interpretation of the terms, assumes that the FOV is much larger than the spatial scale of expected high-frequency fluctuations—in other words, the characteristic scale of the FOV must be larger than the integral turbulent length scale expected to cause fluctuations. Under those assumptions, the average temperature of the image is only affected by a mean trend (warming or cooling) or instrumental effects. The same applies to the temporal length of the TST recording, which must be significantly longer than the duration of expected fluctuations.

2.2.2 Integral statistics

From each of the decomposition terms introduced in Section 2.2.1, temporal and/or spatial statistical parameters can be calculated (except for *mtotal*, which is a scalar). The temporal statistics of *ftotal* are notably

Table 2 Summary of terms used in the decomposition scheme

Term	Name	Dimensions	Description
$\langle \overline{T} \rangle = \overline{\langle T \rangle}$	<i>mtotal</i>	Scalar	Spatiotemporal average of the time sequence
$\overline{T^{\square}}(\mathbf{x})$	<i>mpattern</i>	2-D array	Departure of the average temperature of a pixel from the spatiotemporal average of the time sequence
$\langle T \rangle'(t)$	<i>mtrend</i>	1-D array	Departure of the average temperature of an instantaneous image from the spatiotemporal average of the time sequence
$T^{\square}(\mathbf{x}, t)$	<i>fpattern</i>	3-D array	Departure of the instantaneous temperature of a pixel from the average temperature of the instantaneous image
$T'(\mathbf{x}, t)$	<i>ftrend</i>	3-D array	Departure of the instantaneous temperature of a pixel from the average temperature of that pixel
$\overline{T^{\square}}(\mathbf{x}, t) - \overline{T^{\square}}(\mathbf{x})$ $T'(\mathbf{x}, t) - \langle T \rangle'(t)$	<i>ftotal</i>	3-D array	Spatiotemporal departure of a pixel from both the spatial and temporal mean

useful. The temporal standard deviation of f_{total} is defined as

$$\sigma'_{f_{total}}(\mathbf{x}) = \sqrt{\langle (T'(\mathbf{x}, t) - \langle T \rangle'(t))^2 \rangle} \tag{11}$$

and results in an image that quantifies for each pixel (\mathbf{x}) the integral variability of the temperature fluctuation over a given time period. Note that the prime above the sigma indicates that this is the temporal standard deviation of f_{total} (as there is also an instantaneous spatial standard deviation which is not used). Similarly, a temporal skewness of the temperature fluctuations can be defined:

$$Sk'_{f_{total}}(\mathbf{x}) = \left(\frac{\overline{T'(\mathbf{x}, t) - \langle T \rangle'(t)}}{\sigma'_{f_{total}}} \right)^3 \tag{12}$$

These statistics will be used to quantify the fluctuations and are correlated against thermal, material, and urban form parameters. In the current study, all integral statistics ($\sigma'_{f_{total}}$, $Sk'_{f_{total}}$) were calculated for a time period of 20 min. $\sigma'_{f_{total}}$ and $Sk'_{f_{total}}$ of four 20-min blocks were then averaged in each run (80 min). Based on spectral analysis (Section 2.2.3), 20 min was considered to be short enough to exclude a significant influence by the diurnal course of differential warming and cooling of surfaces, yet long enough to include effects of turbulent exchange of larger eddies. Similarly, statistics can be applied to a spatial field in order to quantify spatial variability. Note that the FOV of the camera does not allow an unbiased sampling and so effects of view geometry and thermal anisotropy (Voogt and Oke 1998) will limit the practical use of the spatial statistics. The spatial standard deviation of $m_{pattern}$, for example, is defined as

$$\sigma_{m_{pattern}}^{\square} = \sqrt{\langle T^{\square 2}(\mathbf{x}) \rangle} \tag{13}$$

Note that the dot-in-a-box symbol above the sigma indicates that the term is a spatial standard deviation. And similarly for the spatial skewness:

$$Sk_{m_{pattern}}^{\square} = \left\langle \left(\frac{\overline{T^{\square}(\mathbf{x})}}{\sigma_{m_{pattern}}^{\square}} \right)^3 \right\rangle \tag{14}$$

2.2.3 Spectral analysis

To quantify the temporal scale of fluctuations in more detail, a Fourier transform was applied to the entire 80 min of f_{total} in each run. All pixels were transformed into temporal spectral energies in 16 different logarithmically spaced bands, using a standard fast Fourier transform, after applying a linear detrending to the time series (Stull 1988). This resulted in images (\mathbf{x}) of the spectral densities in different bands.

2.2.4 Spatial coherence

To quantify the spatial scale (spatial extent) of temperature fluctuations in the image, cross-correlations of the temperature time-series (f_{total}) were calculated between neighboring pixels:

$$C'_{f_{total}}(\mathbf{x}, \mathbf{r}) = \frac{\langle (T'(\mathbf{x}, t) - \langle T \rangle'(t))(T'(\mathbf{x} + \mathbf{r}, t) - \langle T \rangle'(t)) \rangle}{\sigma'_{f_{total}}(\mathbf{x}) \sigma'_{f_{total}}(\mathbf{x} + \mathbf{r})} \tag{15}$$

$C'_{f_{total}}$ will indicate if neighboring pixels, displaced by a distance \mathbf{r} , experience similar fluctuations in their time series of f_{total} . $C'_{f_{total}}$ is useful to quantify any spatial coherence in fluctuations and to assess if any observed coherence relates to surface materials, surface form, and/or residual sensing element geometry (potential effects of calibration/shutter). Practically, for

Table 3 Manual classification of surfaces in the field of view

Surface	n (pixels)	% of FOV	No. of contiguous areas	Median slope (°)
Roof – tile	4,955	6.5	45	34
Roof – gravel	1,535	2.0	15	0
Roof – tar	1,806	2.4	16	30
Roof – metal	1,776	2.3	2	11
Wall – painted	4,304	5.6	37	90
Wall – brick	2,664	3.5	23	90
Ground – roads	1,675	2.2	21	1
Ground – grass	1,406	1.8	10	2
Trees – deciduous	12,662	16.5	33	
Trees – coniferous	1,797	2.3	13	
Excluded	284	0.4	4	
Unclassified	41,936	54.6		

Table 4 Integral parameters for all pixels in the FOV (except for the ones listed as excluded) in comparison to 2 m air temperature

Parameter		Day		Night	
		D1	D2	N1	N2
		Leaves-off	Leaves-on	Leaves-off	Leaves-on
Air temperature (2 m)	(°C)	20.4	16.7	12.5	11.8
$mtotal$	(°C)	24.3	23.8	12.9	12.1
$\sigma_{mpattern}^{\square}$	(K)	3.8	6.1	1.1	1.4
$SK_{mpattern}^{\square}$	(K)	1.16	0.93	-0.35	-0.57

each pixel, the correlation to its neighboring pixels (displaced by \mathbf{r}) was calculated for cardinal directions (left, up, right, down), and the average correlation in all four directions is shown. C'_{ftotal} was calculated for $\mathbf{r} = 1, 2, 4, 8,$ and 16 pixels over periods of 20 min. Note that the actual distance on the ground varies between 0.5 and 2.5 m per pixel displacement due to the oblique sensor view. C'_{ftotal} ranges between 1 (perfect spatial correlation) to -1 (perfect negative correlation), and 0 indicates no correlation with fluctuations of nearby pixels.

2.3 Surface classification and 3-D data

All pixels in the FOV were manually classified by visual (subjective) analysis of rectified (oblique) photos from the camera's location, with the help of the 3-D building model and aerial photos. Four overarching form-based *facet categories* were identified—(a) roofs, (b) walls,

(c) ground, and (d) trees. The categories were further separated based on their facet material into *material classes*. Roofs were separated into classes “tile,” “tar,” “metal,” and “gravel”; walls into “brick” and “painted” (painted stone or concrete); ground into “road” (impermeable) and “lawns”; and trees into “deciduous” and “evergreen” (Fig. 1d; Table 3). Pixels were only classified if they contained the same surface material across the pixel. To avoid neighboring effects, all masks were cropped using a 3×3 erosion filter. For trees, crown areas were classified but not stems. Only trees that were easily identifiable in the leaves-on runs were included; 284 pixels (0.4% of the FOV) were removed from further analysis because they contained either low-emissivity materials or A/C and heat venting systems with significant anthropogenic heat release. The removed areas are listed as “excluded” in Fig. 1d and are not used in any reported statistics or visualizations; 45.4% of all pixels in the FOV were classified into one of the masks. The remaining 54.6% are either pixels

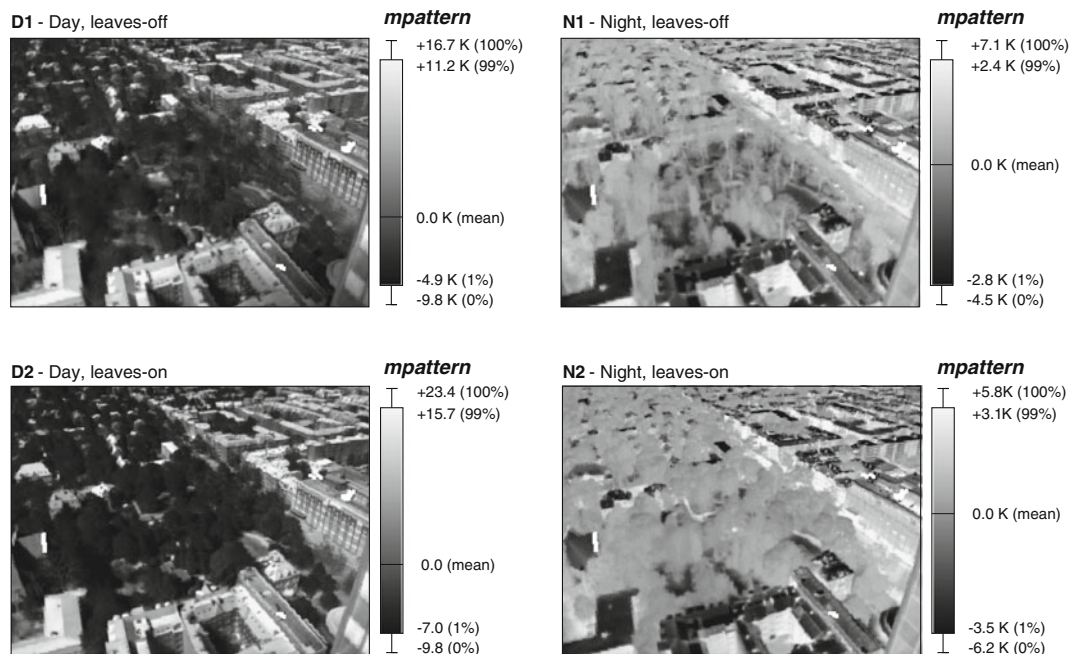


Fig. 2 Spatial temperature anomaly ($mpattern$) of all four runs. The visualization uses a linear grey scale between the 1 and 99th percentile in each image. Pixels drawn in white have been excluded from analysis

with mixed materials, part of the high-rise building’s facade in the lower right foreground (excluded), or areas that had fine structure and were eroded by the 3×3 filter (in the background).

Each TST pixel is linked to the corresponding DSM via 3-D geometrical transformations used in computer graphics (Foley and van Dam 1984), ground control points, and the interior and exterior orientation parameters of the camera. Further details are described in Meier et al. (2011). The combination of FOV and DSM attributes a height above ground, a slope, and an azimuth to each building pixel (roof or wall). Vegetation is not resolved in the DSM, so information on tree crown geometries is not available.

3 Results

We will report temperature fluctuations in relation to facet materials (Section 3.1), to height above ground (Section 3.2) and azimuth (thermal anisotropy, Section 3.3). Those results will then be discussed in Section 4.

3.1 Effects of surface materials

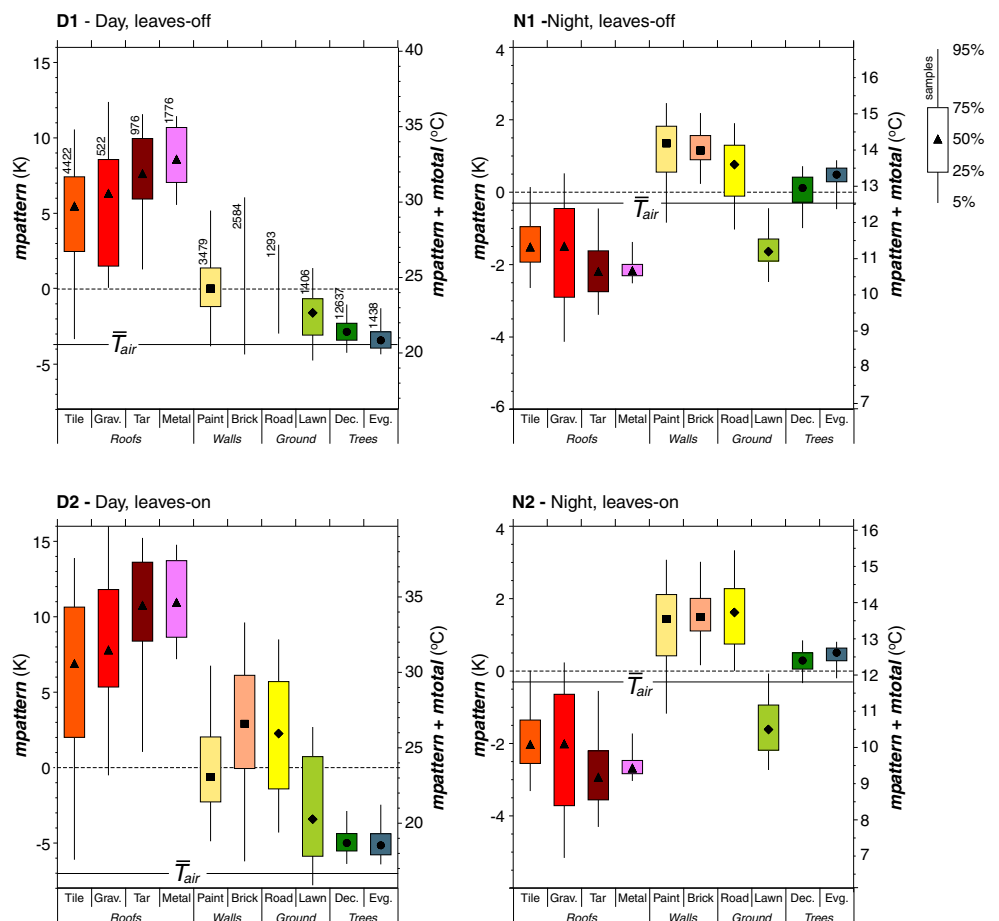
3.1.1 Mean temperatures

Spatial differences in mean temperatures are not the focus of this study, yet they are essential for understanding the magnitude of temperature fluctuations.

The average spatiotemporal temperatures ($mtotal$) for all four runs are summarized in Table 4. $mtotal$ is above air temperature (at 2 m) in the daytime runs (D1 and D2) and close to air temperature in the nocturnal runs (N1 and N2).

The spatial temperature departure ($mpattern$) is shown as images in Fig. 2 for all four runs. Figure 3 shows statistics of $mpattern$ conditionally sampled for each of the facet materials. In the daytime runs (D1 and D2), trees, lawns, and shadowed walls experience the lowest average temperatures. In contrast, roofs, sunlit walls, and street surfaces show the highest average temperatures. The distribution of $mpattern$ ($Sk_{mpattern}^{\square}$) in D1 and D2 is positively skewed toward higher temperatures (Table 4). The daytime median values for $mpattern$ of several roof types ranges between $+5$ K

Fig. 3 Ensemble averages of spatial temperature anomaly ($mpattern$) sorted by facet material in all four runs. The numbers in the upper left graph indicate the number of pixels included in each class and are the same for all four runs



and +11 K. Trees show the lowest temperatures of all material classes and are close to, yet above, air temperatures.

During the night (N1 and N2), roofs and lawns show the lowest temperatures and are typically 1–2.5 K below air temperature. In contrast, wall and road surfaces are the warmest and 1–2 K above air temperature. Trees are closest to air temperature. $m_{pattern}$ in the FOV is negatively skewed ($Sk_{m_{pattern}}^{\square}$; Table 4), indicating that there are more extreme departures from m_{total} for cooler surfaces.

3.1.2 Integral standard deviation of temperature fluctuations

Integral standard deviation of $\sigma'_{f_{total}}$ is shown as images (\mathbf{x}) for all runs in Fig. 4, and statistics for the different facet material classes are summarized in Fig. 5. In both daytime runs (D1, D2), metal roofs show the highest $\sigma'_{f_{total}}$ of all surface materials (label 1 in Fig. 4) and show temperature fluctuations that are nearly twice as strong as for any other observed material. Tile, tar, and gravel roofs show intermediate $\sigma'_{f_{total}}$ (label 2). In both daytime runs, painted (stone and concrete) walls have the lowest $\sigma'_{f_{total}}$ (label 3), followed by brick walls. Fluctuations on vegetation pixels are intermediate

(label 4) and comparable to those on non-metal roofs. Figure 4 illustrates how $\sigma'_{f_{total}}$ of deciduous trees (in the park) changes from the leaves-off situation (D1), where mostly fluctuations on the ground (lawns) are visible, to higher fluctuations of the trees' crowns in the leaves-on situation (D2). Note that coniferous trees have not changed their relative signature compared to other materials (Fig. 5, D1 and D2). In both runs, lawns show the highest $\sigma'_{f_{total}}$ of all vegetated areas (label 5). Special cases are roads where traffic lanes are characterized by a high $\sigma'_{f_{total}}$ (label 6). At night (N1, N2), the only surfaces with noticeable elevated $\sigma'_{f_{total}}$ are lawns (label 7) and trees in N2. Again a clear difference between the leaves-off (N1) and leaves-on (N2) situation is evident in the park where trees in N2 are set apart from the rest of the image (label 9). In Fig. 4, walls are visible as areas that have a lower $\sigma'_{f_{total}}$ than the average of the image (label 8).

Figure 6 shows time series of sample pixels representing each of the classes. Temperature fluctuations over 60 min for the runs D1 and N1 are plotted at 1 Hz and compared to air temperature at 5-min intervals. The graph illustrates the fundamental differences between day (D2) and night (N2). The daytime situation is characterized by a wide range of temperatures and significant fluctuations at multiple frequencies in all traces, while during night temperatures are more

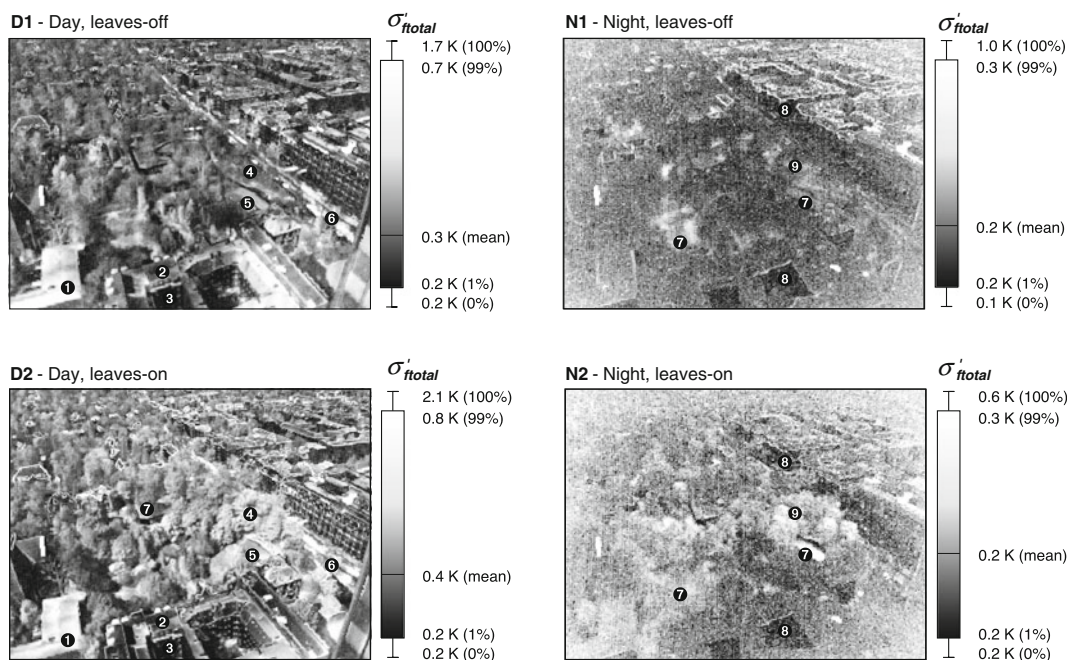


Fig. 4 Average standard deviation of temperature fluctuations ($\sigma'_{f_{total}}$) over 20 min visualized for all four runs. The visualization uses a non-linear gray scale between the 1 and 99th percentile

in each image. Pixels drawn in white have been excluded from analysis. For labels 1–9, see text

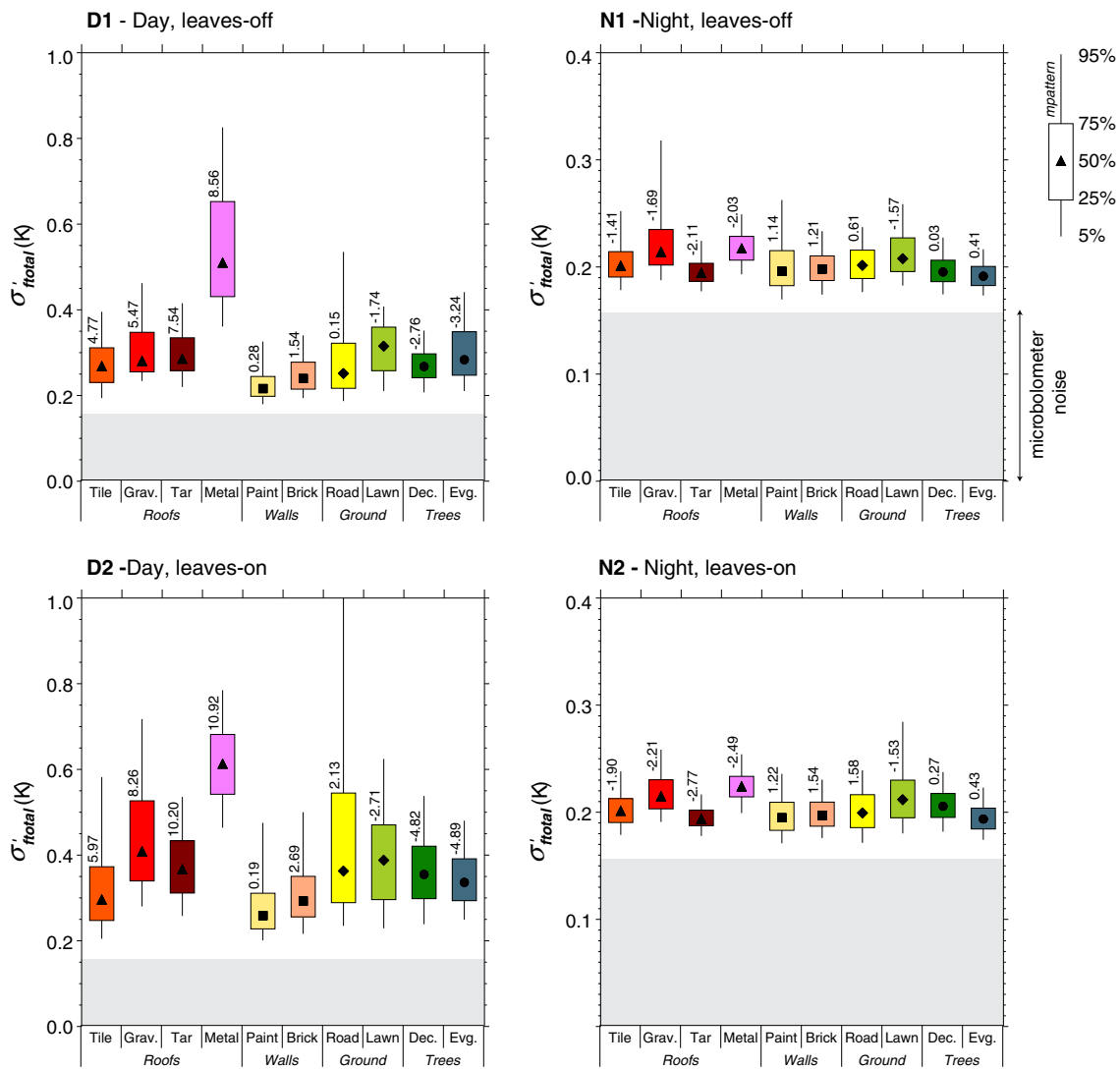


Fig. 5 Ensemble averages of the standard deviation of temperature fluctuations (σ'_{ftotal}) sorted by facet materials in all four runs. The numbers in the upper left graph correspond to the median

m_{total} of each class. The numbers of samples are similar to Fig. 3. The gray-shaded area is the baseline sensor noise as discussed in “Appendix A1”

uniform, and fluctuations are restricted to small scale (high frequency).

3.1.3 Spectral analysis of temperature fluctuations

Figure 7 summarizes spectral energies of temperature fluctuations (f_{total}) for different bands of the Fourier transform of each pixel (\mathbf{x}). The selected images range over three orders of magnitude, between periods of $P = 5$ s to about $P = 500$ s (columns). At the highest frequencies ($P = 5$ s), the spectral energy of the images is rather uniform across them, exceptions being lanes on roads where vehicles move (label 1) and paths in the park where pedestrians walk (label 2). Note that roads

are partially obscured by leaves that emerged in runs D2 and N2 and so traffic is not as easily visible as in D1 and N1. Also noticeable are border effects, i.e., pixels on building edges or between contrasting surfaces are characterized by higher energy—in particular in run D2. Runs N1 and N2 reveal a radial pattern, with lower spectral energies in the center of the image compared to the corners.

At intermediate frequencies ($P = 50$ s), spectral energies of f_{total} show significant differences between D1 and D2. In particular, foliage on trees with large leaves in D2 causes an increase in spectral energy of f_{total} (label 3) compared to other materials and the leaves-off situation, where only a few conifers and

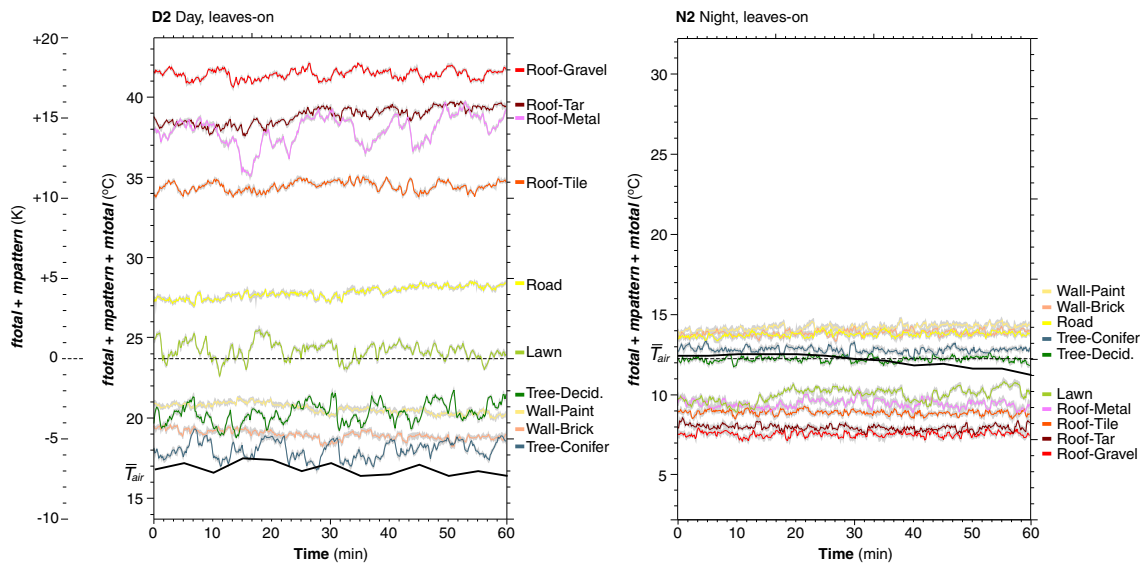


Fig. 6 Sample time series of temperature fluctuations during 60 min of a day (D2) and a night (N2) of selected pixels representing typical behavior for the facet material classes. All pixels are exposed to direct solar irradiance. Values are expressed relative

to the anomaly ($f_{total} + m_{pattern}$, left axis—which is common for both graphs) and absolute temperature ($f_{total} + m_{pattern} + m_{total}$, individual in both graphs)

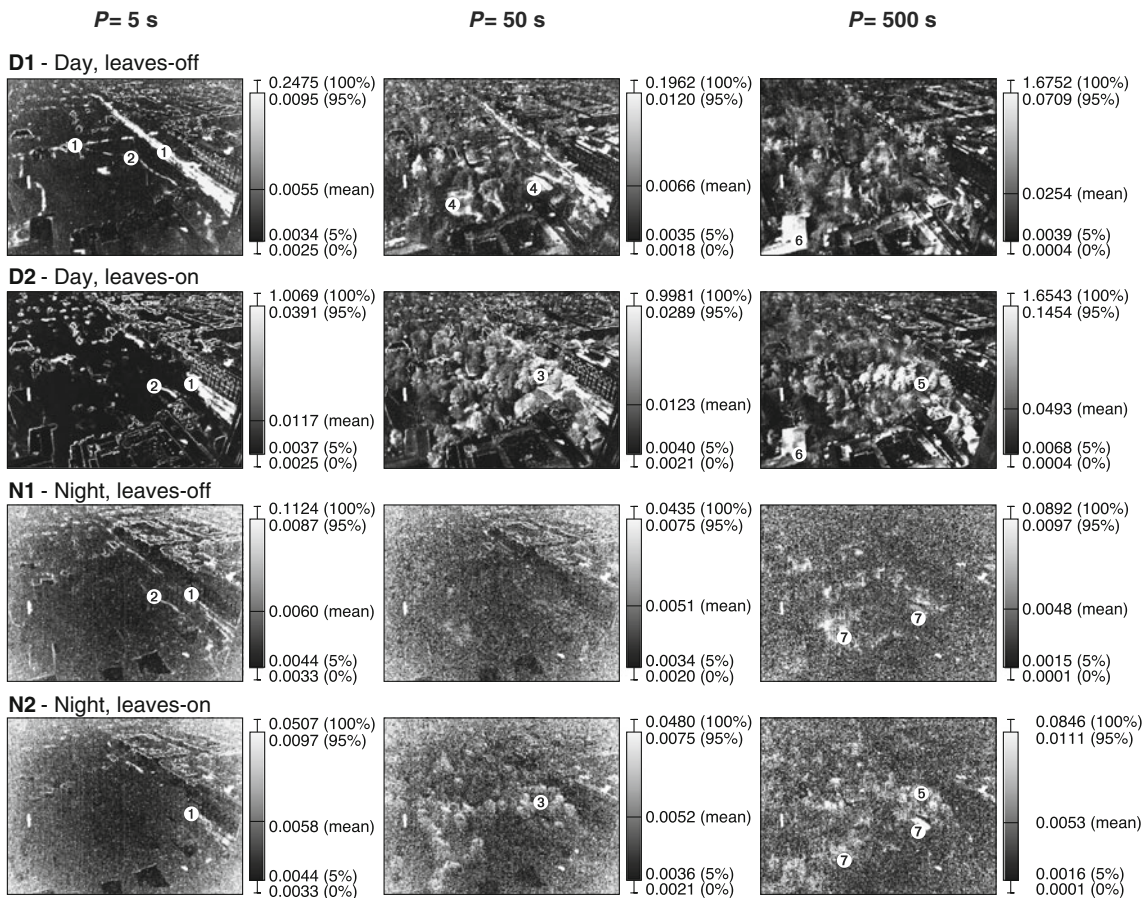


Fig. 7 Normalized spectral energies $fS(f)$ of temperature fluctuations (f_{total}) for all runs (rows) for three selected different bands with period $P = 5, 50,$ and 500 s (columns). The visualiza-

tion uses a linear gray scale between the 1 and 99th percentile in each image. Pixels drawn in white have been excluded from analysis. For labels 1–7, see text

lawns (label 4) stand out. A similar pattern is observed during night, with tree crowns in the center of the park showing larger spectral energies (label 3 in N2), although overall energy in the fluctuations is lower.

At low frequencies ($P = 500$ s), spectral energies reveal a more complex pattern, with gradients across objects. For example, trees in D2 show a clear difference between the south-facing and north-facing parts of crowns (label 5). The highest fluctuations are observed for metal roofs (label 6). During the night, fluctuations are weak and only a few tree crowns (label 5) and lawn patches (label 7) stand out.

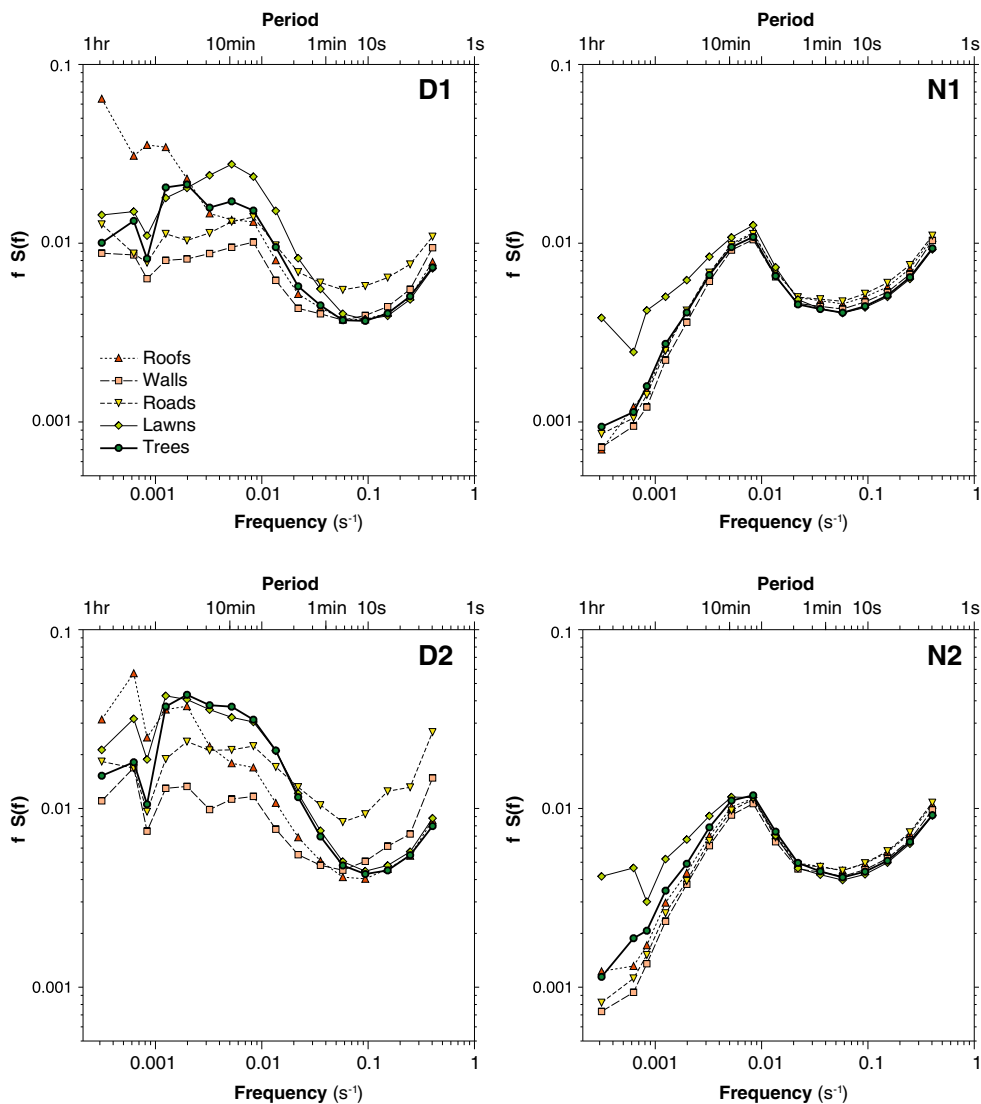
Figure 8 shows ensemble spectra of temperature variations (f_{total}) for different facet categories in 16 logarithmically spaced bands from 1 s to 1 h. The curves shown are median values of each category. All

spectra show a relative minimum around 30 s (50 s at night) and a peak in the range 2–10 min. Spectra stratify into different surface categories above ~ 30 s, with the highest fluctuations for lawns and trees. Notable is the convergence of the spectra between trees and lawns from the leaves-off situation (D1) to the leaves-on situation (D2), where the two classes overlap. On the high-frequency end (right), all materials converge below 10 with increasing energy, the exception being roads, which stay above any other category throughout the high-frequency end at day.

3.1.4 Coherence of fluctuations

Figure 9 visualizes the spatial coherence $C'_{f_{total}}$ of all runs, and Fig. 10 summarizes ensemble statistics of

Fig. 8 Ensemble averaged spectral energy $S(f)$ of temperature fluctuations (f_{total}) for all pixels, multiplied by frequency f . The spectra have been classified into five main facet categories



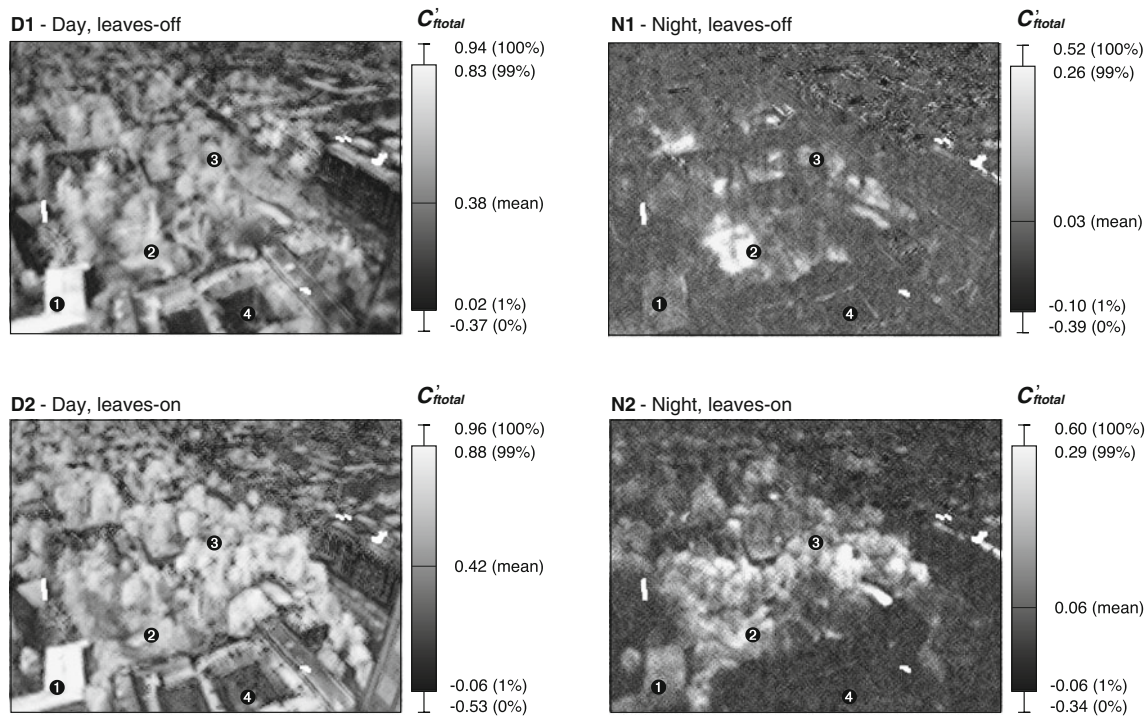


Fig. 9 Spatial coherence C'_{total} of temperature fluctuations at $r = 2$ pixels over 20 min. The visualization uses a linear gray scale between the 1 and 99th percentile in each image. Pixels drawn in *white* have been excluded from analysis. For labels 1–5, see text

C'_{total} sorted by material class. C'_{total} was calculated based on Eq. 15 and quantifies how well the temperature fluctuations of a pixel correlate with its neighbors at a distance of $r = 2$ pixels. The strongest spatial correlation is found on metal roofs (e.g., label 1), followed by tar roofs. But also vegetated surfaces show a significant C'_{total} that reveals the form of individual crowns and lawn patches (lawns—label 2, deciduous tree crowns—label 3 in Fig. 9). Walls (e.g., label 4) or roads show little cross-correlation. During the night, most surfaces are not well correlated, with the exception of clearly visible lawn patches in the park (label 2). Similar patterns have been observed for distances of $r = 1, 4, 8,$ and 16 pixels (not shown).

3.2 Effects of urban form

3.2.1 Mean temperatures vs. height above ground

Figure 11 shows average temperatures and temperature fluctuations as a function of height above ground for walls and roofs. The height above ground was extracted for all pixels from the 3-D city model (Section 2.3). Only data from the leaves-off situation is shown in Fig. 11 to reduce possible interference with vegetation. During the day, temperatures ($m_{pattern}$) of walls

and roofs are above air temperatures and increase with height (Fig. 11a). During the night, temperatures decrease with height. Although lower walls stay significantly warmer than air temperatures, the difference between surface and air temperature is reduced with height. Roofs are all significantly cooler than air temperatures, and also their temperature generally decreases with height (Fig. 11d).

3.2.2 Temperature fluctuations vs. height above ground

Temperature fluctuations on walls are small. Nevertheless, during both the daytime (Fig. 11b) and nighttime (Fig. 11e), a small increase of σ'_{total} with height can be identified. Skewness Sk'_{total} increases from more negative numbers on lower walls to values close to zero in the middle and higher part of walls. Such a trend is not observed for roofs, where effects of slope are likely included.

3.3 Effects of thermal anisotropy

Microscale temperature patterns created by the 3-D urban surface structure, as well as by the thermal properties of urban surfaces, lead to directional variations

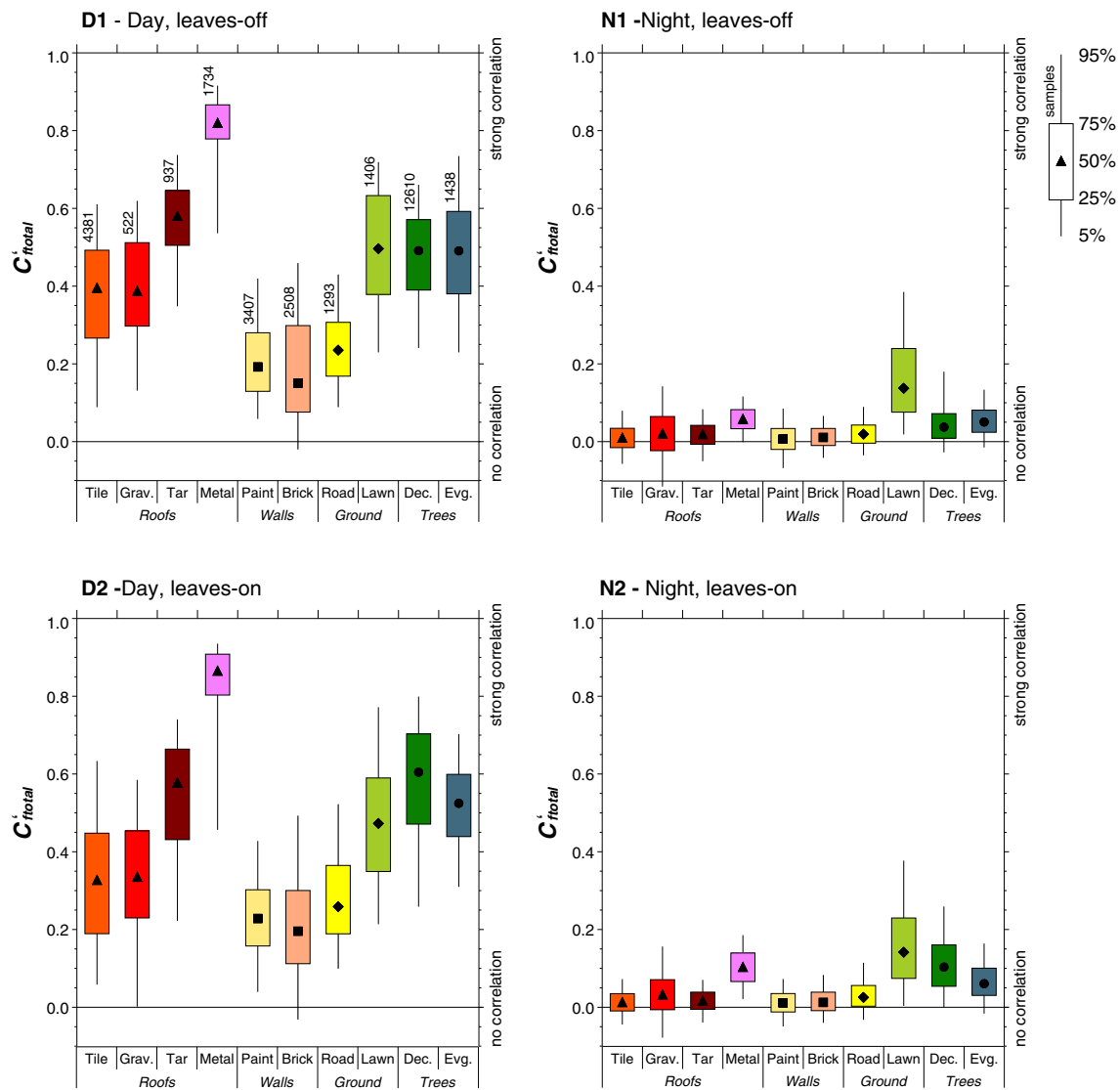


Fig. 10 Ensemble averages of the spatial coherence at $r = 2$ pixels (C'_{ftotal}) sorted by facet materials in all four runs. The numbers in the upper left graph indicate the number of pixels included in each class and are the same for all four runs

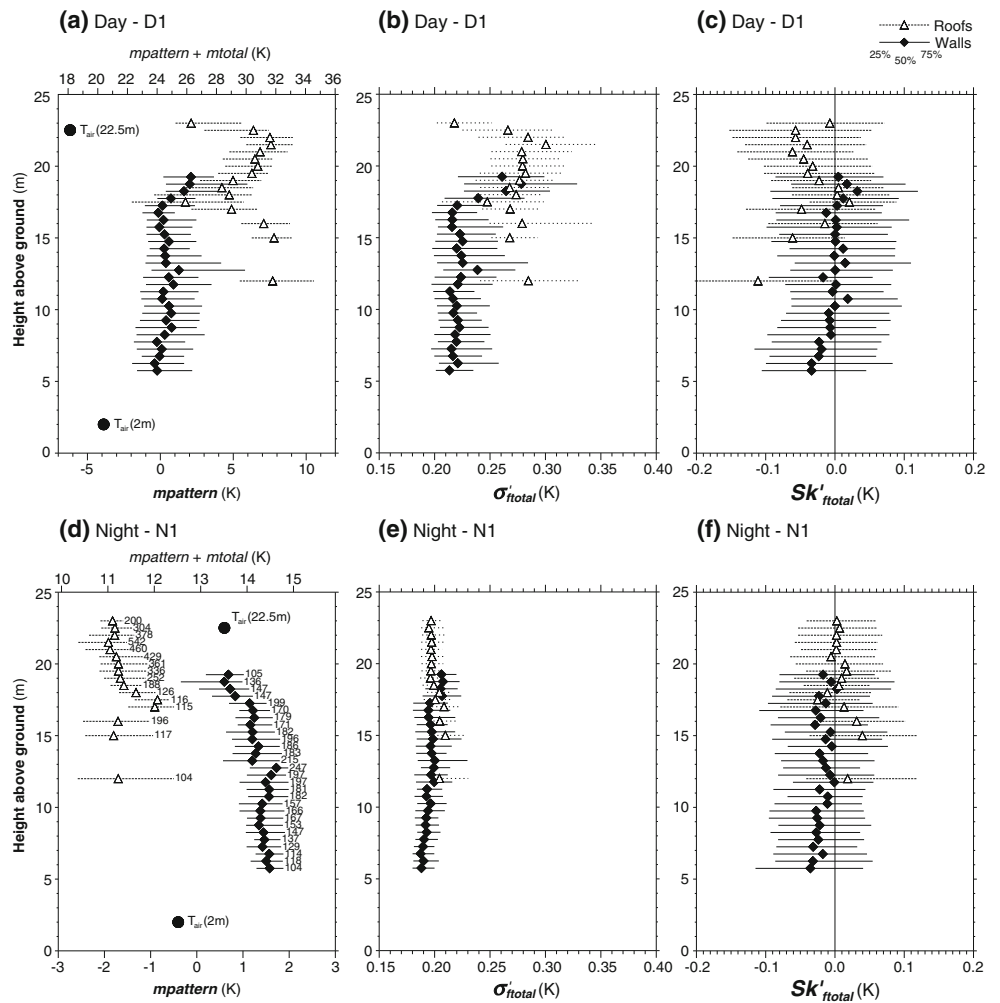
of long-wave emittance. This directional variation is termed effective thermal anisotropy (Voogt and Oke 2003). The application of TIR remote sensors from a fixed FOV to the determination of surface temperatures is complicated by effective thermal anisotropy (Lagouarde et al. 2004). The term “effective” is used in order to indicate that anisotropy arises because of surface structure and temperature patterns, rather than the non-Lambertian behavior of individual facets (Voogt 2008).

Figure 12 shows the effects of the effective anisotropy on mean temperatures and fluctuations. The rectangular street grid in the FOV is aligned along $120/300^\circ$ and $30/210^\circ$, respectively. Most building walls

and roofs have therefore an azimuth of 30° (NNE), 120° (ESE), 210° (SSW), or 300° (WNW). Walls with an azimuth towards WNW are hidden in the current FOV and not sampled by the camera (which points toward 325°). These walls are therefore not represented in Fig. 12. However, the camera can tangentially see roofs with an azimuth of around 300° that have a gentle slope. This applies mostly to the foreground.

While most NNE-facing walls are slightly below air temperature in the daytime runs, walls facing ESE and SSW are 3–6 K warmer than air temperatures (Fig. 12a). For roofs, NNE-facing facets are the coolest and SSW-facing facets are the warmest. A similar pattern is found for D2. The nighttime runs (N1,

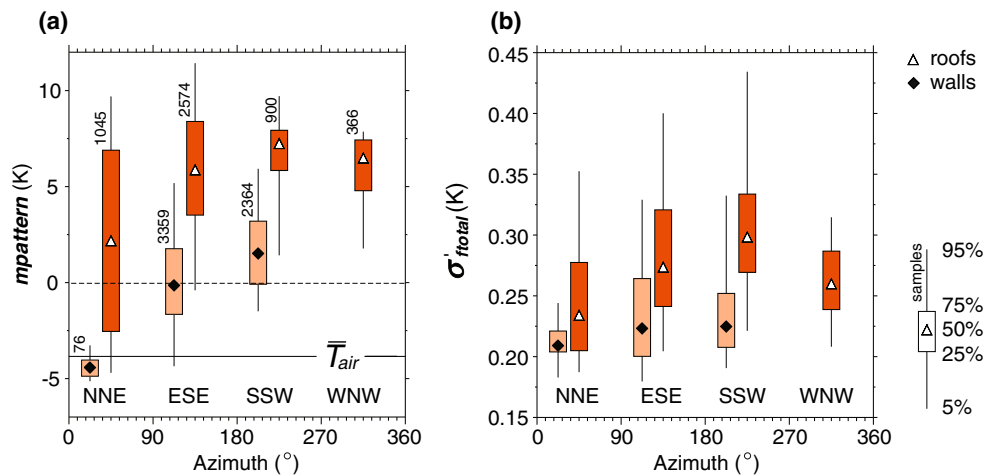
Fig. 11 Height dependence of **a, d** spatial temperature anomaly ($m_{pattern}$), **b, e** standard deviation of temperature fluctuations (σ'_{total}), and **c, f** skewness of temperature fluctuations (Sk'_{total}) of walls (brick and paint) and roofs (all materials except metal) the two leaves-off runs (D1 and N1). Numbers in **e** are the number of pixels considered in each class and are the same for all other figures. Only classes with more than 100 pixels are shown



N2) do not show any directional variability of roofs, while north facing walls are about 1.5 K cooler in the evening than south facing ones (not shown). Temperature fluctuations expressed as σ'_{total}

do not change significantly with azimuth for walls (Fig. 12b). Roofs show anisotropy in the magnitude of fluctuations, where the highest fluctuations are found on SSW facing roofs and the lowest on NNE facing roofs.

Fig. 12 Dependence of **a** spatial temperature anomaly ($m_{pattern}$) and **b** standard deviation of temperature fluctuations (σ'_{total}) of walls and roofs as a function of geographic azimuth. Numbers in **a** refer to the number of pixels included in the analysis. All data are from run D1 (roofs 15° slope and metal roofs excluded)



4 Discussion

Observed fluctuations in temperature (f_{total}) will be discussed in terms of the energy balance at the surface itself. The effect of instrumental noise of the microbolometer array and effects along the line of sight are quantified in “Appendix A1” to “Appendix A5” as those are not central to the method developed here. Although instrumental effects explain a significant part of the observed total variation of $\sigma'_{f_{total}}$, none of those instrumental effects can explain the differences observed between material classes or the observed relations with height and azimuth of the urban form. Those differences must be an effect of the surface energy balance of the corresponding facets. It was hypothesized that net all-wave radiation, Q^* , laminar boundary-layer and aerodynamic resistances (r_b and r_a), subsurface heat storage (expressed as thermal admittance), and potentially water availability control the magnitude and spectral characteristics of both the mean temperature and the temperature fluctuations of a facet.

4.1 Radiation and shadowing

In runs D1 and D2, surfaces situated higher above the ground received more direct short-wave radiation for a longer period over the morning which explains that the spatial temperature departure ($m_{pattern}$) is significantly above air temperature for roofs and higher walls (Fig. 11a). In contrast, lower surfaces are more likely in shadow and are below or at air temperature. During the night, the influence of a reduced sky-view factor on the long-wave radiation exchange is suitable to explain higher temperatures of lower walls compared to higher walls (Fig. 11d). Notable are extraordinarily warm walls in narrow courtyards (foreground in Fig. 2, N1 and N2) and walls in the denser part of the city (Fig. 2, upper right). As urban form does not change over 20 min, sky-view factor and solar access can explain mean temperatures and warming/cooling rates, but not fluctuations.

In the daytime runs, moving shadows, however, could create temperature fluctuations on a range of scales. The thermal effect of shadows and accompanied reduced or increased solar irradiance is not a high-frequency phenomenon caused by the atmosphere, matching our hypothesis. However, it has been shown that depending on the duration of shadowing, the scale of the object causing shadows, and the change in short-wave radiation, the persistence of shadow effects varies from several minutes to hours (Meier et al. 2010). Shadows reduce the difference between surface and air

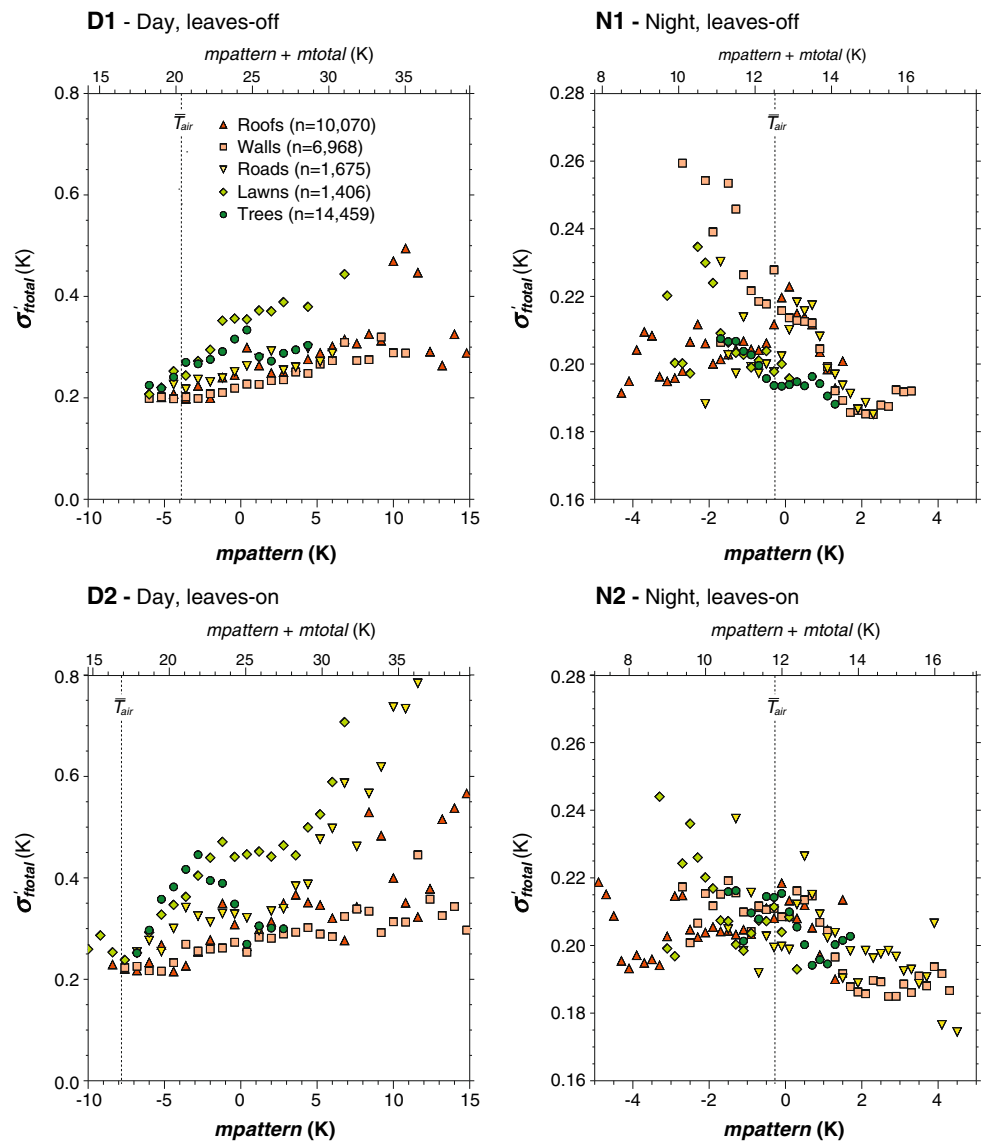
temperatures; hence, it is expected that shadowed parts of the FOV show lower fluctuations due to turbulent exchange. This is illustrated in Fig. 12, where north facing roofs and walls have lower mean temperatures and also less temperature fluctuations $\sigma'_{f_{total}}$.

4.2 Turbulent heat transfer

Figure 13 plots fluctuations ($\sigma'_{f_{total}}$) against mean temperature ($m_{pattern}$) for five overarching categories (roofs, walls, roads, lawns, trees). For D1 and D2, clear positive relationships between mean temperature and fluctuations develop—the warmer a surface (the higher the difference to air temperature), the higher are the observed temperature fluctuations ($\sigma'_{f_{total}}$). Temperatures of surfaces that are significantly warmer than air temperature are more affected by turbulent exchange. If cooler air from the atmosphere is mixed toward the surface, it will cause stronger fluctuations at the surface, and part of the sensible heat is transferred into the air, which cools the surface. Interestingly, the different categories in Fig. 13 show varying slopes (vegetation shows a steeper slope, roofs intermediate, walls do not show a clear relation). This could suggest that material properties such as thermal admittance, but also water availability, and potentially form factors (laminar boundary layer thickness) may play an important role (see Section 4.4). The role of water availability is evident in the temperatures of vegetated surfaces that transpire, which are on average (D1) and (D2) lower than roofs (Fig. 3). This is in agreement with Leuzinger et al. (2010) who found in an urban environment at similar latitude daytime differences in temperatures of ~ 20 K between roofs and trees. Observed fluctuations change most dramatically with increasing difference to air temperature for trees and lawns compared to artificial materials that have no Q_E during D1 and D2. The separation in Fig. 13 is in part attributed to the fact that not only sensible heat flux but also latent heat flux causes fluctuations at high frequencies (note the significant vapor pressure deficit in the runs, Table 1).

Over rough surfaces, turbulent exchange between the surface and the atmosphere is intermittent. A few eddies that occur in a short fraction of the time are responsible for the majority of the sensible heat flux. During daytime, the mean surface temperature \bar{T} of most urban facets is higher than the air temperature \bar{T}_{air} . Urban facets stay generally at a high surface temperatures and are only sporadically lowered by the few eddies bringing a lower air temperature T_{air} close to the surface. This pattern causes the surface temperature trace to experience sporadic strong negative departures

Fig. 13 Standard deviation of temperature fluctuations ($\sigma'_{f_{total}}$) as a function of spatial temperature anomaly ($m_{pattern}$) for all pixels classified into four facet categories (roofs, walls, roads, lawns, roads, and trees). T_{air} is the measured air temperature at the climate station (2 m). In particular during night, actual T_{air} is expected to be highly variable in space

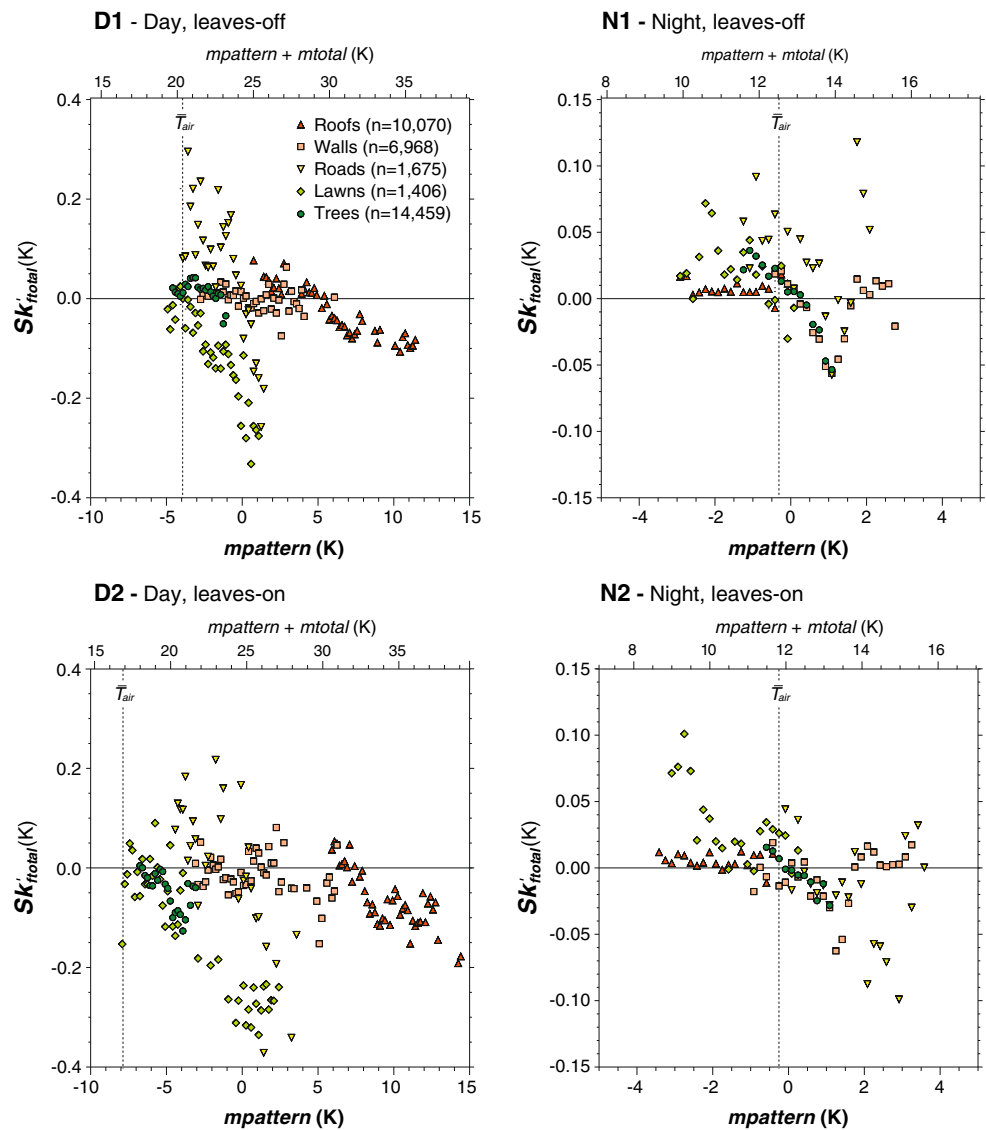


(i.e., a negative skewness, $Sk'_{f_{total}} < 0$). The opposite would be expected for surfaces that have a surface temperature $T < T_{air}$ which would experience a positive $Sk'_{f_{total}}$ when sporadically warmer air is moved over the cooler surface. This pattern is sustained because air is thermally better mixed than surfaces, and the range of observed surface temperatures of the urban surface is much larger than the range in air temperature in the urban canopy. Figure 14 illustrates $Sk'_{f_{total}}$ as a function of mean temperature ($m_{pattern}$) and in relation to air temperature. In daytime runs (D1, D2), most materials (lawns and roofs, to some extent also trees) show decreasing (i.e., more negative) skewness with increasing departure from air temperature. Walls do not show a clear trend of $Sk'_{f_{total}}$ with temperature.

Roads show a positive $Sk'_{f_{total}}$, likely due to contamination by “warm” moving vehicles (see “Appendix A4”). During nighttime, in particular tree and lawn surfaces show positive $Sk'_{f_{total}}$ when below air temperature and negative $Sk'_{f_{total}}$ when above.

Another notable detail is the height dependence of $Sk'_{f_{total}}$ —walls below 10 m show a more negative $Sk'_{f_{total}}$ compared to walls that are closer to the mean building height (~ 18 m) and where $Sk'_{f_{total}} \sim 0$ (Fig. 11c, f). We postulate that if an eddy with an air temperature T_a (during day and night below the surface temperature of walls) approaches a wall, this will cause a drop in the wall surface temperature of ΔT . For an eddy of given energy, ΔT is expected to be of roughly the same magnitude on top of the walls compared to the bottom

Fig. 14 Skewness of temperature fluctuations ($Sk'_{f_{total}}$) as a function of temperature anomaly ($m_{pattern}$) for all pixels classified into the four main facet material categories (roofs, walls, lawns, roads, and trees)



of the walls because the mean surface temperature of the walls does not vary with height above ground (see Fig. 11a) and the material properties are constant with height (constant high thermal admittance). However, the significant difference postulated between top of wall and bottom of wall is the frequency of occurrence of eddies that causes mixing. Christen et al. (2007) show for turbulence in a comparable urban setting that the integral length scale of velocity fluctuations as well as the intermittency of sensible heat flux exchange is the lowest just at roof height and increases in both directions, i.e., down into the canopy and up into the higher roughness sublayer, where eddies responsible for exchange become less frequent. At roof level, where turbulence is characterized by small-scale and frequent eddies caused by the shear layer, $Sk'_{f_{total}}$ stays close to

zero. In the sheltered bottom of the urban canopy, but also in the atmosphere above the mean shear layer (exposed roofs > 20 m), eddies are infrequent and $Sk'_{f_{total}}$ consequently experiences a more negatively skewed distribution away from the principal shear layer.

4.3 Thermal admittance

Why are the slopes of $\sigma'_{f_{total}}$ vs. mean temperature ($m_{pattern}$) in Fig. 13 not similar for different categories? This could be explained by surface and subsurface properties, namely the different thermal admittance μ of surface materials. A facet with a high thermal admittance (e.g., walls or roads) “accepts” any heat flux caused/enabled by turbulent exchange quickly and efficiently and, as a consequence surface temperatures,

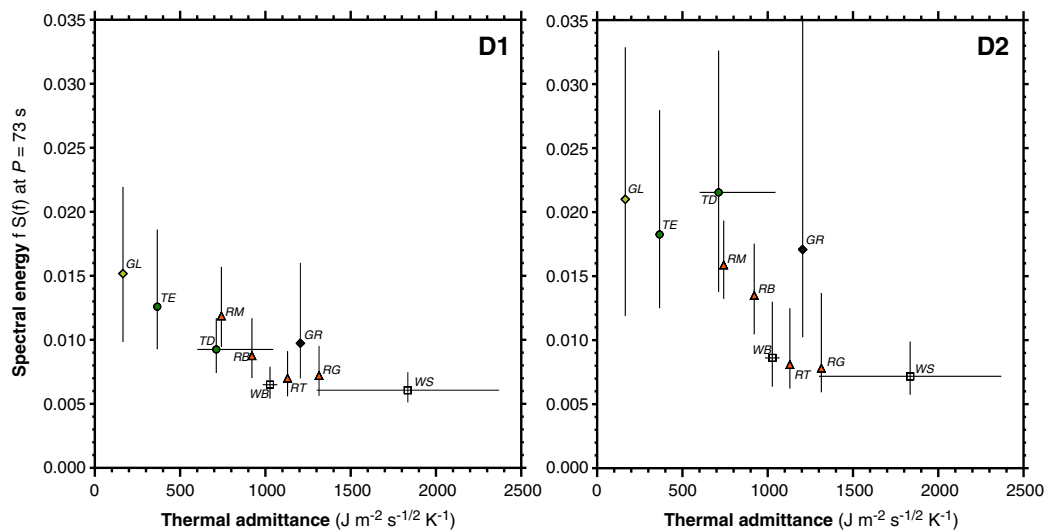


Fig. 15 Ensemble averaged spectral energy of temperature fluctuations (f_{total}) at $P = 73$ s as a function of literature values for thermal admittance μ of different facet materials. Vertical error bars denote the 25 and 75th percentiles of all pixels in the given material class. Horizontal error bars, if given, refer

to the range of values provided in the literature. Legend: *RT* roofs—clay tiles, *RG* roofs—gravel, *RB* roofs—bitumen/tar, *RM* roofs—metal, *WB* walls—brick, *WS* walls—stone/paint/concrete, *GL* ground—lawns, *GR* ground—roads, *TD* trees—deciduous, *TE* trees—evergreen

do not change dramatically. Facets with a low thermal admittance (e.g., leaves, porous lawn canopies), however, respond to a change in Q_H with a significant surface temperature change (or Q_E).

Figure 15 shows the relationship between μ and spectral energy at $P = 73$ s, the range where spectra start to significantly diverge between materials (Fig. 8). Values for thermal admittance are taken from the literature describing the thermal properties of building materials (Oke 1981; Spronken-Smith and Oke 1999; Berge et al. 2009) and of vegetation (Byrne and Davis 1980; Jones 1992; Jayalakshmy and Philip 2010). Where several estimates exist in these sources, the horizontal error bars in Fig. 15 indicate the range of values reported. A relationship between temperature fluctuations and thermal admittance is evident (D1 and D2), resulting in higher fluctuations on materials with lower thermal admittance—although the level of fluctuations is different (which is also influenced by the magnitude of radiative and turbulent exchange).

4.4 Spatial scale of turbulent exchange fluctuations

The spatial coherence of fluctuations expressed by C'_{ftotal} (Figs. 9 and 10) indicates that the spatial scale of fluctuations is more evident on surfaces that experience significant fluctuations. There is a relatively constant sensor noise across the microbolometer array (“Appendix A1”) on which the energy balance effects (as other error sources) are superimposed. Therefore, it is not surprising that for pixels where (uncorrelated)

sensor noise is dominant and actual fluctuations expected from the energy balance are small (high thermal admittance materials), C'_{ftotal} is close to zero. However, if fluctuations are dominantly caused by the surface energy balance, then C'_{ftotal} is expected to be higher (closer to 1) as turbulent eddies exist on a range of scales, and some will affect neighboring pixels at the same time. It is clear that the spatial and temporal resolution of the system limits the information that can be extracted on the scales explicitly resolved, and temperature fluctuations caused by small eddies (less than ~ 1 m) will not be resolved. Nevertheless, it is notable how clearly different surfaces separate in C'_{ftotal} . In particular, the lawn surfaces, with an excellent response due to their lower thermal admittance, show spatially coherent patterns, suggesting that large coherent eddies (30 s to several minutes) control most of the exchange of heat over a rough surface as reported from traditional fast anemometry (e.g., Roth and Oke 1993; Feigenwinter and Vogt 2005; Christen et al. 2007).

5 Conclusions

This contribution presents a scheme to separate a TST dataset into mean and fluctuating signals. The proposed decomposition scheme was applied to surface temperatures from four TST datasets in a complex urban environment over 80 min. The chosen FOV was an urban surface composed of many different facets (roofs, walls, trees, lawns, roads). Facets in the FOV

experienced fluctuations in surface temperature that related to surface materials and form. The observed relationships can be summarized as follows:

- Surfaces that experience the strongest surface temperature fluctuation are significantly warmer (cooler) than air temperature. Surfaces that are closer to air temperature show less fluctuation (see Fig. 13).
- With increasing temperature of a surface above air temperature, fluctuations show a stronger negative skewness. There is also some evidence for the opposite case, where surfaces with surface temperature below air temperature show a more positive skewness. This is explained by large turbulent eddies that cause sensible heat to be exchanged between a more uniformly mixed atmosphere and a thermally patchy surface.
- Surface materials with lower thermal admittance (lawns, leaves) show higher fluctuations in surface temperature than surfaces with high thermal admittance (walls, roads) (see Fig. 15). Leaf emergence of deciduous trees between runs shows impact on high-frequency thermal behavior. The emerged leaves cause surface temperatures to fluctuate more compared to a leaves-off situation.
- The spatial coherence of fluctuations suggests that the relevant scale of atmospheric turbulence might be significantly larger than the geometric resolution of the image (0.5–2.5 m).

Although a significant part of the fluctuations in apparent surface temperatures are caused by sensor noise, sensor calibration effects, and other complicating factors (changes in atmospheric transmission, small lateral movements of the camera due to wind, moving objects, see the “Appendix”), the key findings let us conclude that the effect of turbulent exchange of sensible heat between different urban facets and the atmosphere on the surface temperature signal can be measured in the time traces of most materials.

Clearly, there are spatial and temporal constraints that limit the study to processes inside the spatiotemporal scale the field observation was designed for. The smallest fluctuations observable with the current geometric resolution were 0.5 m (in the foreground). However, more recent work (Christen and Voogt 2010) has demonstrated that significant temperature fluctuations can happen at much smaller scales (10 cm). An upper spatial limit is the scale of the entire FOV. The effect of large-scale boundary layer eddies that could change surface temperatures of the entire image are filtered by the decomposition scheme and are not visible either.

Further, the temporal scale of resolved fluctuations is limited. Although the nominal operation frequency was 1 Hz, the highest frequencies are significantly contaminated by sensor noise. In this range, the temperature resolution of the sensor and sensor effects formed a severe limitation. In particular in the nocturnal runs, where the thermal structure of the atmosphere and the absent short-wave irradiance are expected to reduce surface temperature fluctuations, a separation of sensor effects from energy balance effects is impossible for most surfaces—except metal roofs and lawns.

Nevertheless, the current study underlines the potential of using high-frequency thermal remote sensing in energy balance and turbulence studies at complex land–atmosphere interfaces. Using high sampling frequencies in TST observations allows for the extraction of information on the dynamic response of the surface energy balance to atmospheric turbulence, thermal admittance of surface materials, and/or potentially visualizes turbulent motions. This is possible in complex canopies such as urban environments where a direct measurement of fluxes and/or turbulent exchange in a spatial context is otherwise not possible.

Acknowledgements The infrastructure and the experimental part of this study were funded by “Energy eXchange and Climates of Urban Structures and Environments (EXCUSE)” supported by TU Berlin (Scherer). The data analysis and computing infrastructure were supported by the Natural Sciences and Engineering Research Council of Canada (NSERC, discovery grant 342029-07, Christen).

Appendix A: Quantification of error sources

In addition to true changes in surface temperature, the radiance signal could fluctuate due to signal noise of the microbolometer focal plane array (“Appendix A1”), changing temperature gradients (signal drift) across the array as the array progressively warms up or cools down (“Appendix A2”), changing absorption along the LOS (“Appendix A3”), effects of moving objects (“Appendix A4”), vibration of the camera platform (“Appendix A5”), and effects of reflection (“Appendix A6”). Those effects will be separately quantified and/or discussed.

A1 Signal noise of the microbolometer array

To test the noise of the microbolometer array, the same equipment was operated in a controlled temperature chamber at 16°C for 80 min, recording the temperature of a uniformly warm concrete slab (50 × 50 × 4.5 cm) using the same housing, calibration, and recoding set-

tings as outdoors. The measured $\sigma'_{f_{total}}$ in the center of the array was determined as 0.169 K which corresponds to approximately 40–50% of the average $\sigma'_{f_{total}}$ in the daytime runs and 70–75% of the average $\sigma'_{f_{total}}$ in the N1 and N2 runs in form of a random background noise. This means that random inter-pixel noise of the Peltier cooled array is a dominant effect that adds noise on top of the energy-balance driven changes. Nevertheless, sensor noise should not correlate to any specific surfaces in the FOV. Based on the spectral results presented, noise dominates fluctuations in the high-frequency part ($P < 30$ s), where ensemble-averaged spectra of all facet classes converge, and surface effects cannot be separated (see Fig. 8).

A2 Differential warming or cooling of the microbolometer array

The effect of differential warming or cooling across the array is expected to be eliminated constantly by the internal calibration (shutter) but might add additional high-frequency noise at higher frequencies than the shutter. Differential warming or cooling is expected to cause more variability on the corners of the array compared to its thermally more stable center. Indeed, N1 and N2 runs show a radial pattern with slightly lower $\sigma'_{f_{total}}$ in the center compared to the corners (Fig. 4). In the temperature controlled chamber run, $\sigma'_{f_{total}}$ increases by 0.050 K from 0.169 K in the center to 0.219 K in the corners, which corresponds $\sim 15\%$ of the average signal of $\sigma'_{f_{total}}$ during the day and $\sim 24\%$ during night. The effect is more evident in higher frequencies, i.e., the spectral analysis (Fig. 7, N1 and N2) reveals this radial effect clearly at a period of 5 s.

Patterns in the cross-correlation functions $C'_{f_{total}}$ that relate to the image geometry could be a further indicator of fluctuations caused preferably in certain regions of the image (e.g., corners). Although interesting patterns relating to the actual surface objects are revealed by $C'_{f_{total}}$ (Section 3.1.4 and Fig. 9), none of the patterns shows a dependence on distance from image center or in any specific direction across the array.

A3 Absorption in the turbulent atmosphere along the line of sight

To estimate the effect of air temperature and humidity fluctuations along the LOS, an atmospheric radiative transfer model (MODTRAN 5.2; Berk et al. 2005) was combined with the sensor's known spectral sensitivity (see Meier et al. 2011 for details). Using measured standard deviations of temperature and humidity fluctuations (see Section 2.1.3 and Table 2), an

upper limit of the effect of a turbulent atmosphere was estimated as follows: The maximal error is considered as the difference between modeled atmospheric absorption for two temperatures that were offset by $\sigma_{T_{air}}$ at absolute air temperature T_{air} . The estimated effect of air temperature fluctuations along the median path length of 234 m is 0.018 K for N1 and 0.012 K for N2. During daytime, due to a strongly convective atmosphere, stronger fluctuations of T_{air} are observed that cause maximum fluctuations of 0.068 and 0.073 K for D1 and D2, respectively. This corresponds in all cases to less than 10% of the measured signal of $\sigma'_{f_{total}}$. Note that the calculation assumes that air temperatures will change instantaneously along the entire line of sight as expressed by $\sigma_{T_{air}}$. But realistically, temperature variations (eddies) will cause the spatially integrated value of $\sigma_{T_{air}}$ along the LOS to be much smaller than the single-point measurement of $\sigma_{T_{air}}$. Similarly, the effect of humidity fluctuations was estimated as the difference between modeled atmospheric absorption for the same temperature, but different absolute humidity (offset by σ_{ρ_v} , see Table 2) at the measured absolute humidity ρ_v . Effects of humidity fluctuations along the path are in all cases $< 3\%$ of measured $\sigma'_{f_{total}}$.

A4 Moving objects along the LOS

The approach presented in this study assumes that all objects in the FOV are fixed and not moving. However, in an urban environment, cars and pedestrians (which are usually warmer) trace temperature signals that are either directly resolved or cause sub-pixel variation. Higher-order moments and the spectral analysis at high frequencies (Fig. 7 at $P = 5$ s) indeed indicate extreme values along road lanes that are attributable to moving traffic. Also ensemble spectra of road surface temperatures are higher in the range of 1–30 s compared to any other surfaces (Fig. 8).

Further, wind causes flexible objects (trees) to move. A displacement, even in the sub-pixel scale, would change the signal emitted from pixels and can also alter the geometry of surface objects. Tree movement was not monitored, but studies indicate that at the observed wind speed of ~ 2.5 m s⁻¹, the unimodal swaying of typical coniferous trees is less than 1 m at 15-m height (Schindler et al. 2010).

A5 Moving of the camera

Finally, the camera itself (mounted on a 3-m boom) or the entire high-rise building might sway relative to the ground. This would lead pixels that are on strong mean gradients (such as edges) to show higher $\sigma'_{f_{total}}$ due to

contamination by neighboring pixels, yet affect the entire image. Evidence for this effect is observed in Figs. 4 (D2) and 7 (D2, and N1, most clearly visible at 5 s). To quantify this error, an edge detection filter was applied to calculate the spatial standard deviation of $m_{pattern}$ in a 3×3 neighborhood ($\sigma_{3 \times 3}$), which is an indication of the sharpness of nearby “edges.” $\sigma_{3 \times 3}$ was then compared to the temporal $\sigma'_{f_{total}}$ on a pixel-by-pixel basis. For the entire image, there is positive relationship between $\sigma_{3 \times 3}$ and $\sigma'_{f_{total}}$ with slopes of 0.008 K K^{-1} ($r^2 = 0.01$) in D1, 0.044 K K^{-1} ($r^2 = 0.32$) in D2, 0.025 K K^{-1} ($r^2 = 0.07$) in N1, and 0.009 K K^{-1} ($r^2 = 0.03$) in N2. These relationships are estimated to explain 2.6% of $\sigma'_{f_{total}}$ in D1, 6.4% in D2, 9.0% in N1, and 1.6% in N2. This matches the visual interpretation of the images, where runs D2 and N1 are more affected by this error. While wind speed was similar during the two daytime and the two nighttime runs, wind direction was changing from along the boom (view direction, 325° in D1 and N2) to perpendicular in N1 and N2 (Table 1). A perpendicular wind is expected to cause more lateral swaying of the boom and/or building and hence more displacement. If the same procedure is applied only to the masked areas that are at least 1 pixel away from any facet edge, the explained error is reduced to 1.2% (D1), 4.5% (D2), 4.7% (N1), and 0.7% (N2) of $\sigma'_{f_{total}}$ because sharp edges are excluded.

A6 Reflectivity

Most materials studied have emissivities <1.0 and part of the signal in the apparent surface temperature might be caused by reflection of fluctuating radiance from nearby objects or the sky. As large fluctuations of the long-wave emittance (originating from nearby objects, the sky or the long-wave part of the direct solar irradiance) are not expected, an error from reflection is likely small. The only exception could be a non-Lambertian behavior of a surface (e.g., metal roof) in combination with a changing solar position over 20 min. Evidence for this effect was not found in the current dataset.

References

- Ballard JR, Smith JA, Koenig GG (2004) Towards a high temporal frequency grass canopy thermal IR model for background signatures. *Proc SPIE* 5431:251–259
- Berge B, Butters C, Henley F (2009) *The ecology of building materials*, 2nd edn. Architectural, London, 427 pp
- Berk A, Anderson GP, Acharya PK, Bernstein LS, Muratov L, Lee J, Fox MJ, Adler-Golden SM, Chetwynd JH, Hoke ML, Lockwood RB, Cooley TW, Gardner JA (2005) MODTRAN5: a reformulated atmospheric band model with auxiliary species and practical multiple scattering options. *Proc SPIE* 5655:88–95
- Byrne GF, Davis JR (1980) Thermal Inertia, thermal admittance and the effect of layers. *Remote Sens Environ* 9:295–300
- Chazdon RL (1988) Sunflecks and their importance to forest understorey plants. *Adv Ecol Res* 18:1–63
- Christen A, van Gorsel E, Vogt R (2007) Coherent structures in urban roughness sublayer turbulence. *Int J Climatol* 27:1955–1968
- Christen A, Voogt JA (2010) Inferring turbulent exchange processes in an urban street canyon from high-frequency thermography. Recorded presentation of the 19th symposium on boundary layers and turbulence, 2–6 Aug 2010, Keystone CO, USA
- Chudnovsky A, Ben-Dor E, Saaroni H (2004) Diurnal thermal behavior of selected urban objects using remote sensing measurements. *Energy Build* 36:1063–1074
- Feigenwinter C, Vogt R (2005) Detection and analysis of coherent structures in urban turbulence. *Theor Appl Climatol* 81:219–230
- Foley JD, van Dam A (1984) Fundamentals of interactive computer graphics. In: *The Systems Programming Series*, 1st edn. Addison-Wesley, Reading
- Garai A, Kleissl J, Smith SGL (2010) Estimation of biomass heat storage using thermal infrared imagery: application to a walnut orchard. *Boundary Layer Meteorol* 137:333–342
- Katul GG, Schiedge J, Cheng-I H, Vidakovic B (1998) Skin temperature perturbations induced by surface layer turbulence above a grass surface. *Water Resour Res* 34:1265–1274
- Kolbe TH (2009) Representing and exchanging 3-D city models with CityGML. In: Lee J, Zlatanova S (eds) *Lecture notes in geoinformation and cartography*. Springer, Berlin, pp 15–31
- Hoyano A, Asano K, Kanamaru T (1999) Analysis of the sensible heat flux from the exterior surface of buildings using time sequential thermography. *Atmos Environ* 33:3941–3951
- InfraTec (2005) Operating instruction for VarioCAM[®] head. InfraTec GmbH, Gostritzer Straße 61–63, 01217 Dresden, Germany
- Jayalakshmy MS, Philip J (2010) Thermophysical properties of plant leaves and their influence on the environment temperature. *Int J Thermophys* 31:2295–2304
- Jones HG (1992) *Plants and microclimate—a quantitative approach to environmental plant physiology*, 2nd edn. Cambridge University Press, Cambridge, 428 pp
- Jones HG (1999) Use of thermography for quantitative studies of spatial and temporal variation of stomatal conductance over leaf surfaces. *Plant Cell Environ* 22:1043–1055
- Lagouarde JP, Moreau P, Irvine M, Bonnefond JM, Voogt JA, Sollicie F (2004) Airborne experimental measurements of the angular variations in surface temperature over urban areas: case study of Marseille (France). *Remote Sens Environ* 93:443–462
- Leuzinger S, Körner C (2007) Tree species diversity affects canopy leaf temperatures in a mature temperate forest. *Agric For Meteorol* 146:29–37
- Leuzinger S, Vogt R, Körner C (2010) Tree surface temperature in an urban environment. *Agric For Meteorol* 150:56–62
- Meier F, Scherer D, Richters J (2010) Determination of persistence effects in spatio-temporal patterns of upward long-wave radiation flux density from an urban courtyard by means of time-sequential thermography. *Remote Sens Environ* 114:21–34
- Meier F, Scherer D, Richters J, Christen A (2011) Atmospheric correction of thermal-infrared imagery of the 3-D urban

- environment acquired in oblique viewing geometry. *Atmos Meas Tech* 4:909–922
- Monteith JL, Unsworth MH (2008) *Principles of environmental physics*, 3rd edn. Academic, New York, 418 pp
- Oke TR (1981) Canyon geometry and the nocturnal heat island: comparison of scale model and field observations. *J Climatol* 1:237–254
- Paw-U KT, Brunet Y, Collineau S, Shaw RH, Maitani T, Qiu J, Hipps L (1992) On coherent structures in turbulence above and within agricultural plant canopies. *Agric For Meteorol* 61:55–68
- Raupach MR, Shaw RH (1982) Averaging procedures for flow within vegetation canopies. *Boundary-Layer Meteorol* 22:79–90
- Roth M, Oke TR (1993) Turbulent transfer relationships over an urban surface. I. Spectral characteristics. *Q J Roy Meteorol Soc* 119:1071–1104
- Schindler D, Vogt R, Fugmann H, Rodriguez M, Schonbörn J, Mayer H (2010) Vibration behavior of plantation-grown Scots pine trees in response to wind excitation. *Agric For Meteorol* 150:984–993
- Shimoda S, Oikawa T (2008) Characteristics of canopy evapotranspiration from a small heterogeneous grassland using thermal imaging. *Environ Exp Bot* 63:102–112
- Spronken-Smith RA, Oke TR (1999) Scale modelling of nocturnal cooling in urban parks. *Boundary-Layer Meteorol* 93:287–312
- Stull RB (1988) *An introduction to boundary layer meteorology*. Kluwer Academic, Dordrecht, 670 pp
- Sugawara H, Narita K, Mikami T (2001) Estimation of effective thermal property parameter on a heterogeneous urban surface. *J Meteorol Soc Jpn* 79:1169–1181
- Voogt JA (2008) Assessment of an urban sensor view model for thermal anisotropy. *Remote Sens Environ* 112:482–495
- Voogt JA, Oke TR (1997) Complete urban surface temperatures. *J Appl Meteorol* 36:1117–1132
- Voogt JA, Oke TR (1998) Effects of urban surface geometry on remotely-sensed surface temperature. *Int J Remote Sens* 19:895–920
- Voogt JA, Oke TR (2003) Thermal remote sensing of urban climates. *Remote Sens Environ* 86:370–384